NMR spectroscopy of electroceramics – Applications to lead-free perovskite oxides

Groszewicz, Pedro B.

DOI
10.1016/j.oceram.2021.100083

Publication date
2021

Document Version
Final published version

Published in
Open Ceramics

Open Ceramics 5 (2021) 100083

Contents lists available at ScienceDirect

Open Ceramics

journal homepage: www.editorialmanager.com/oceram

NMR spectroscopy of electroceramics – Applications to lead-free perovskite oxides

Pedro B. Groszewicz

Department of Radiation Science and Technology, Delft University of Technology, Delft, 2629JB, Netherlands

A B S T R A C T

Understanding about the local structure plays an increasing role for the discovery of structure-property relations in electroceramics. Despite that, characterization techniques dedicated to the local structure are still not widespread in the electroceramics community. Nuclear magnetic resonance spectroscopy (NMR) has the potential to close this gap, as particularly sensitive to minute distortions and well-suited for the structural analysis of partially disordered materials, such as solid-solutions. This review aims at an introduction of this technique tailored to the materials scientist. Following a brief description of the base concepts, its capabilities are demonstrated by a series of tangible examples from local structural questions pertinent to materials based on three classes of lead-free perovskites, namely $BaTiO_3$, $NaNbO_3$ and $Na_{1/2}Bi_{1/2}TiO_3$. Beyond its application to lead-free perovskite oxides, the concepts illustrated here are of broad interest for further oxides and materials in general.

1. Introduction

Electrically functional materials with piezoelectric properties have long been known and find application in a broad range of devices. Examples of these materials are the market-leading $Pb(Zr,Ti)O_3$ (PZT), as well as $Pb(Mg_{1/3}Nb_{2/3})O_3$ (PMN), together with a plethora of solid solutions, with which their properties can be engineered [1]. Despite their advantageous piezoelectric properties, these lead-based compositions are not environmentally friendly, owing to their lead content and increasingly restrictive legislation motivates the search for alternative materials.

Research effort has focused on substitute materials with environmentally acceptable compositions. It resulted in a class of lead-free piezoelectric ceramics, which in the same way as their lead-based counterparts, exhibits a perovskite structure. Bismuth sodium titanate - $(Bi_{1/2}Na_{1/2})TiO_3$ (BNT) - accounts for one of the base compositions in this class of materials, alongside with solid solutions based on $NaNbO_3$ (NN) [2,3], and compositions based on $BaTiO_3$ (BT) [4].

Their functional properties are intimately connected to their atomic arrangements. Especially for solid solutions, discrepancies between the average and local structure can be significant. Understanding about the local structure has played an increasing role for the discovery of structure-property relations in electroceramics ranging from relaxor ferroelectrics to battery materials. By relying only on conventional characterization methods, these important traits and connections might remain concealed and hinder the further development of functional materials.

For crystalline materials, the macroscopic structure precisely reflects the structure on the atomic scale. A good example are table salt crystals, which cubic shape reflects the symmetry of an ordered arrangement of ions throughout its lattice. This ordered arrangement goes down to the unit cell and the very coordination environment of each sodium cation by six chloride anions, a trait of the local structure of NaCl.

A sharp contrast to this situation would be a glass, as for example a borosilicate glass, which exhibits a distribution of bond lengths and angles in a disordered fashion. Despite the lack of long-range order, its structure, and the way it is connected to properties, can be defined in terms of the local structure [5]. Examples are specific local environments for boron in either tetragonal BO_4 or trigonal-planar BO_3 units, the interconnectivity between SiO_4 tetrahedra, or next-near neighbours around network formers.

Whereas the long-range order found in crystalline compounds is best analysed by means of diffraction methods, with a widespread use of powder X-ray diffraction in particular, this technique has limitations to characterize structural disorder and reveal traits of the local structure. Furthermore, perovskite oxides often display small deviations from cubic aristotype, which involve displacement of light oxygen atoms in the anion sub-lattice, or either lack long-range coherence for cation displacements.

An increasing number of materials rely on structural disorder for their functional properties. The large response of relaxor ferroelectrics to external stimuli, as electric field or mechanical stress, has its origin on disordered displacements of ions within its lattice. Relaxor ferroelectrics with a perovskite structure exhibit an average (macroscopic) structure often perceived as crystalline, whereas their local structure is

E-mail address: p.groszewicz@tudelft.nl.

https://doi.org/10.1016/j.oceram.2021.100083
Received 1 February 2021; Accepted 2 March 2021
Available online 5 March 2021

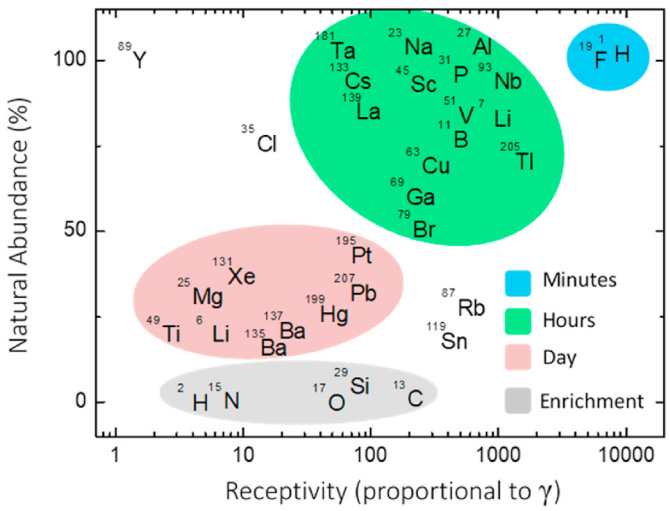

Fig. 1. Common NMR active isotopes sorted by measurement time.

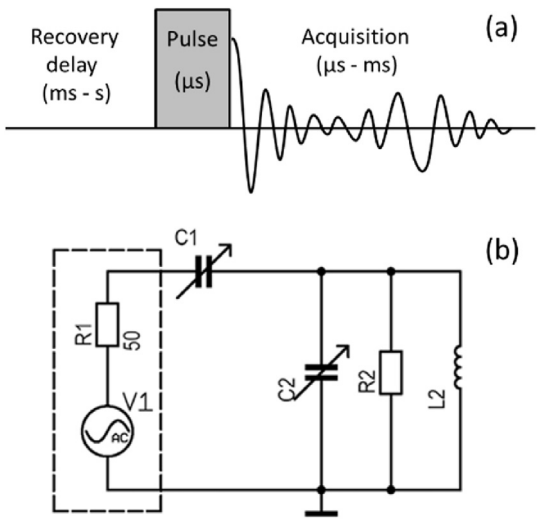

Fig. 2. (a) simple pulse sequence. (b) Schematics of electronic circuit of an NMR probe. Adapted from Ref. [17].

characterized by distinct disorder. The same is valid in general whenever doping and the formation of solid solutions is required to achieved desired properties.

In order to develop a deeper understanding of the structure-property relations in electroceramic materials, it is essential to gain a better insight into their local structure. Solid-state nuclear magnetic resonance (NMR) spectroscopy is *per se* the appropriate technique to accomplish this task, as an additional method to support ceramists and material's scientists in the elucidation of structure-property relations. In nuclear magnetic resonance, the resonance frequency of nuclear spins is a direct function of interactions with their local environment, as for example the chemical shift and the quadrupolar interactions [6]. These nuclear interactions have in common a very short range, which makes NMR independent of the coherence length of structural motifs and very sensitive to minimal distortions of the local structure.

Bearing the characteristics of this spectroscopic technique and the challenges inherent to this class of materials in mind, recent years have witnessed a profusion of applications of NMR spectroscopy of electroceramics materials as ferroelectrics, piezoelectrics, antiferroelectrics and battery materials. In this review, the base concepts of this technique are described, followed by examples from three classes of lead-free perovskite oxides, namely $BaTiO_3$, $NaNbO_3$ and $Na_{1/2}Bi_{1/2}TiO_3$-based materials, which deepen and illustrate the capabilities of this characterization method for the local structure of electroceramics and related materials.

2. Basic concepts of NMR

NMR stands for nuclear magnetic resonance spectroscopy. It relies on the interplay between the magnetic moment of NMR-active nuclei in a sample of interest and the equipment's magnetic fields to detect the so-called Larmor frequency, or a particular distribution of frequencies in form of an NMR spectrum.

Although not every isotope is NMR-active, most elements in the periodic table display stable, NMR-active isotopes. These nuclei exhibit an intrinsic angular momentum, or spin, which is associated to the nuclear magnetic moment (μ) as follows.

$$\mu = \gamma . I \qquad 1$$

where I, the spin quantum number, can take values of 0, 1/2, 1, 3/2, 2, 5/2, …and γ is the gyromagnetic ratio, or the proportionality constant between the former, with an unit of $rad.T^{-1}.\ s^{-1}$. Each isotope has a distinct gyromagnetic ratio [7], due to the specific arrangement of protons and neutrons in its nuclear structure. Structural information results from interactions between the nuclear magnetic moment with magnetic fields generated by surrounding electrons.

In addition to that, NMR-active nuclei with spin $I \geq 1$ (quadrupolar nuclei) also exhibit an electric moment [8]. This characteristic offers an additional source of structural information in NMR spectra via an interaction between the nuclear electric quadrupolar moment and the gradient of the electric field at the nuclear site, which is often treated as a perturbation of the main, magnetic interaction.

Among stable nuclides, protons (^{1}H) have the highest gyromagnetic ratio, with lower values displayed by isotopes commonly found in ceramics such as ^{17}O, ^{23}Na, ^{137}Ba, ^{47,49}Ti and ^{93}Nb, which are examples of quadrupolar nuclei. A further property of interest from NMR-active nuclei is their natural abundance, which has a direct impact on the intensity of the NMR signal. Due to low signal-to-noise ratio intrinsic to the physics of NMR spectroscopy [9], several signal accumulations have to be repeated to record a useful spectrum. Together with the receptivity, a function of γ, the natural abundance majorly dictates the time required for an NMR measurement (Fig. 1). Depending on the nucleus of interest, it may take between a few seconds to a few days for a single measurement, although it may also vary according to sample characteristics as spectrum width and relaxation times.

Whenever subjected to an external magnetic field, the nuclear magnetic moment of NMR-active nuclei ($I \geq 1/2$) behaves in such a way that an oscillatory movement starts. The spin dynamics underlying this phenomenon is well described in the literature [10,11], and it suffices to say that it in much resembles the precession movement of a spinning top. This precession frequency (ω_0), or Larmor frequency, is central to the NMR experiment, and depends both on the magnitude of the external magnetic field (B_0) and the gyromagnetic ratio γ from the particular NMR-active nucleus under study.

$$\omega_0 = \gamma . B_0 \qquad 2$$

where the subscript 0 denotes the spectrometer's static, large magnetic field. Eq. (2) states that the frequency ω_0 depends on the characteristic γ constant, what renders NMR spectroscopy an element-specific characterization method, as frequency ranges for different NMR-active isotopes quite often lie far apart from each other.

Furthermore, with magnetic fields ranging from 7 T to 21 T in commercially available NMR spectrometers to date, the usual NMR frequency lies in the range of tens to hundreds of MHz and scales proportionally to the strength of magnetic field. In NMR jargon, it is common to state the strenght of the spectrometer's magnetic field in terms of the Larmor frequency of ^{1}H in that field, for which case the aforementioned

magnets would be called a 300 MHz and a 1 GHz, respectively. Due to the similar frequency, much of NMR hardware shares commonalities, and stems from, radio electronics.

Besides the onset of a precession frequency ω_0, the external magnetic field B_0 also causes the development of a macroscopic magnetic moment (M_z) in the sample. Manipulation of the M_z vector by action of a second, oscillatory, magnetic field B_1 generated by radio frequency (RF) pulses in a coil surrounding the sample enables the detection of nuclear magnetic resonance signal (free induction decay - FID) and the measurement of an NMR spectrum around the Larmor frequency [12]. This procedure briefly describes a pulse sequence (Fig. 2a) and is repeat several hundreds or thousands of times until sufficient signal is accumulated. A recovery delay precedes every RF pulse to allow for the build-up of sufficient magnetization (M_z) in the sample and enough signal to be collected in every accumulation round (NMR jargon – scan).

The NMR signal is recorded with aid of an RLC resonance circuit Fig. 2b, the probe, in which coil the sample is located. The probe is placed within the room-temperature bore of the cryomagnet (required to generate the strong magnetic fields in use). Such a configuration offers large flexibility for different sample environments, with broad capabilities for *in situ* experiments available, such as variable-temperature [13], electric field [14], orientation [15] or sample atmosphere [16].

2.1. Resonance

In order to observe the nuclear magnetic resonance effect, a sample within an external field B_0 must be excited with a frequency that matches its Larmor frequency. For this purpose, it is customary to employ an alternating magnetic field B_1 perpendicular to B_0. The interaction between B_1 and the sample's magnetic moment can be described classically by equations of motion for the nuclear magnetization (Bloch equations). The later precess about B_0 with angular frequency ω. Under the assumption that the different Zeeman levels are not equally populated, a macroscopic magnetic moment M_z develops parallel to B_0. M_z is the vector sum of the magnetic moment of all spins with respect to the z-axis. The linear oscillating B_1 field can be described as the sum of two vectors $B_{1,left}$ and $B_{1,right}$, which rotate on the xy-plane with opposite directions. In this representation, M_z only interacts with the component of B_1 that displays the same direction of rotation of its precessing magnetic moments.

This interaction may also be regarded in a rotating frame (x',y'z), which has the same angular frequency as ω. In this rotating frame, the B_1 component in question is stationary. As long as the frequency of B_1 matches the Larmor frequency, the M_z vector will be solely under the influence of this B_1 component, and will precess about this magnetic field instead of about B_0. This interaction results in the flipping of the M_z magnetization onto the xy-plane, and is the principle underlying the detection of NMR spectra.

The extent of the precession about B_1 may be expressed in terms of the angle swept by the M_z vector while under the influence of this magnetic field, also known as flip angle θ, for which the following relation is valid:

$$\Theta = \gamma.B_1.\tau_P \quad (3)$$

Here τ_P stands for the duration of the application of B_1. This oscillating magnetic field is produced by the application of an alternated current to a coil that encompasses the sample. As far as pulsed Fourier-transform NMR is concerned, such a current is applied for a short period, in the range of μs to ms, and is, therefore, denoted as a pulse in NMR jargon.

The same coil is employed in the detection of the NMR signal that follows immediately after the application of pulses to the spin-system. As soon as the B_1 field is no longer present, the magnetization vector precesses only under the influence and around B_0. This movement induces an electric current in the NMR coil [12], which can be recorded and processed in order to reveal information about the spin system contained in it.

2.2. NMR probe

The NMR probe can be regarded as an RLC resonance circuit [18]. A resonance circuit is employed in the NMR probe to make use of the advantages of the resonance condition. At the resonance frequency, there is strong amplification of the magnetic field B_1 inside the coil. The resonance circuit, depicted on Fig. 2b consists of a coil of inductance L2 and a tuning capacitor of capacitance C2. The coil is the element responsible for converting electrical power delivered by an RF transmitter into a magnetic field, thereby enabling the interaction with the sample's spin system. The tuning capacitor has a variable capacitance, which results in a tunable resonance frequency (ν_0) for the circuit, according to equation (Eq. (4)). Both of these components may exhibit some losses, which are expressed by the resistance (R), in series to the coil. A variable capacitor (C1) in series to the resonance circuit is also present. This element is known as the matching capacitor, which assures optimal power transfer between the RLC circuit and the transmission line (the RF cable) and further to the RF transmitter.

$$\nu_0 = \frac{1}{\sqrt{(L.C)}} \quad (4)$$

This configuration ensures that the NMR probe is capable of transmitting, on the one hand, of the high power pulses from the spectrometer to the NMR coil, and on the other hand, the weak detected signal further to the spectrometer. As the circuit bears variable matching and tuning capacitors, these two parameters can be varied until ν_0 is adjusted to the Larmor frequency of the nucleus of interest, with an enhanced power transfer between RF transmitter and probe at this frequency. This procedure is informally called "wobbling", and both capacitors are alternately adjusted until the minimum of the reflection of a low power RF signal is located at the carrier frequency of the spectrometer.

2.3. NMR interactions – relation to the local structure

Nuclear magnetic resonance spectroscopy (NMR) is a well-suited tool for the characterization of the local structure of materials, especially for those that show a certain degree of structural disorder. Owing to the short range nature of interactions between the probed nucleus and its near surroundings [6,19] NMR is a structural probe at the atomic scale. Moreover, it does not depend on a long-range crystal order, as every local environment delivers a specific fingerprint, independent of how they are spatially arranged. Nevertheless, such disordered structural features also pose challenges to NMR spectroscopy, as they may result in a distribution of signals resulting from different local environments around the studied nuclei, what may lead to loss of resolution.

NMR spectra are often the result of a convolution of many interactions between the probed nucleus and its surroundings. The most relevant ones for the study of electroceramics are the chemical shift and the quadrupolar interaction. The chemical shift (i.e. shielding) is an interaction between the nuclear spin and a shielding effect caused by surrounding electrons when exposed to an external magnetic field [20]. The quadrupolar coupling is an interaction between the nuclear electric quadrupolar moment and the electric field gradient (EFG) imposed on it by the surrounding charges (i.e. neighbouring ions) [21]. These two interactions will be discussed in more detail in the applications section. Besides them, there is plethora of other interactions, such as dipolar interaction [22], J-coupling [23], and paramagnetic interactions [24], but which play only a minor role for NMR of diamagnetic electroceramics.

Despite the direct connection between NMR parameters and the local structure, the interpretation of NMR spectra in terms of a material's structural features is not unique. Structural models play an important role in clarifying the meaning of NMR parameters as the chemical shift and the electric field gradient for specific classes of materials, especially when structural disorder is present [25]. These models can range from pure

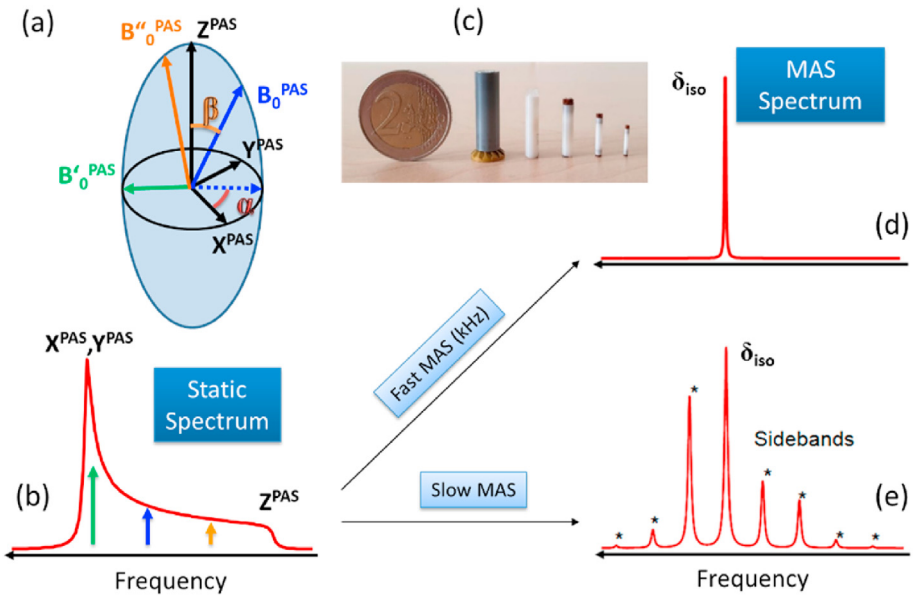

Fig. 3. Tensor depiction of anisotropic NMR interactions. (a) Elipsoid representing an NMR tensor. Coloured arrows depitc different orientations of B_0. (b) Static spectrum observed for a powder sample as consequence of an anisotropic interaction, NMR frequency of crystallites with different orientations depicted by coloured arrows (c) Rotors (i.e. sample containers). Used for magic angle spinning (MAS) NMR (adapted from Ref. [33]). (d) MAS spectrum under fast spinning – only isotropic component is left. (e) MAS spectrum under slow spinning – envelope of spinning sidebands reflect anisotropy present in the static spectrum.

geometric considerations [26] up to calculations with density functional theory (DFT) [27,28].

In cases where contribution from several interactions overlap, one requires advanced, often two-dimensional NMR experiments in order to extract the individual contribution of each interaction (i.e. NMR parameters). Such experiments can be based on the correlation between two interactions, as in the case of the triple-quantum magic angle spinning (3QMAS) NMR experiment [29].

A detailed analysis of NMR spectra allows one to extract structure-related parameters (quadrupolar coupling, chemical shift) by simulating the experimental spectra [30,31]. Ab-initio methods are very helpful to translate NMR parameters into structural information and have had a tremendous increased in precision and availability in the past 5–10 years with codes for solid-state NMR implemented in CASTEP and VASP.

2.4. Orientation dependence of NMR interactions

NMR interactions in solids are anisotropic; their magnitude, and by extension the overall NMR frequency of a given crystallite, is orientation dependent. In general terms, anisotropic interactions in NMR are described by tensors [32], which can be represented by ellipsoids, such as the one in Fig. 3a. NMR tensors are structural properties and thus fixed with respect to the molecular frame (lattice). The relative orientation of NMR tensors and the magnetic field B_0 determines the extent of frequency shift caused by a given NMR interaction, as depicted in a simplistic way by the coloured arrows in Fig. 3a and b. Mathematically, a reorientation of the tensor (or crystallite) within the static magnetic field B_0 is equivalent to a reorientation of the magnetic field within the fixed molecular frame of the tensor, but the latter is much simpler in terms of the matrix operations involved.

The size of a tensor determines the range of frequencies observed in an NMR line under the influence of a given interaction and thus determines the signal width, as for example the frequency difference between a B_0 orientation along Z^{PAS} and X^{PAS}. Moreover, the tensor symmetry is also reflected in the shape of the NMR line in question. To illustrate this point, we take the tensor from Fig. 3c, an axial symmetric tensor (X^{PAS} and Y^{PAS} have equal magnitude), as example. For an isotropic distribution of crystallites, such as in a powder or non-oriented ceramic sample, B_0 orientations along the XY plane of the tensor occur with higher probability than along the Z^{PAS} axis. Hence, the intensity of the NMR line at the frequency of X^{PAS}, Y^{PAS} will be higher than at the opposite edge. Conversely, breaking of the axial symmetry would result in $X^{PAS} < Y^{PAS}$, with a shift of the line's maximum towards its centre and formation of a shoulder at the left edge.

The orientation dependence of an NMR interaction can be averaged under magic angle spinning (MAS) conditions (Fig. 3d) [34]. Samples are spun at frequencies of tens of kHz within the NMR coil, while placed in special samples containers (MAS rotors). Rotors of different sizes can achieve varying rotation speeds, with maximum MAS frequency of 15 kHz for rotors with 4 mm outer diameter and up to 65 kHz with 1.3 mm rotors (Fig. 3c). Rotation is achieved with air bearings and winged rotor caps, driven by pressurized air within the stator that encompasses the NMR coil in MAS NMR probes. If the static signal width in frequency units is broader than the MAS frequency, it is not completely averaged, but modulated by the sample spinning [35]. This modulation results in the splitting of the broad static pattern into an envelope of spinning sidebands (Fig. 3e), separated from each other by a distance equal to the MAS rotation frequency. As signal intensity is concentrated into the spinning sidebands, recording spectra under MAS yields much higher signal-to-noise ratio, enabling the detection of signals in shorter experiment time.

3. NMR of electroceramics – application examples

In the next sections, a selection of examples from the application of NMR spectroscopy in the study of electroceramics is presented, which highlights how local structural information can be extracted from NMR spectra. Although constrained to lead-free perovskite oxides, the concepts illustrated here are of general application and of interest for further oxides and materials in general.

3.1. $BaTiO_3$-based perovskites

Barium titanate exhibits considerable piezoelectric properties and has been discovered in the early 1940's as the result of an effort to develop new, ceramic-based, dielectric materials as a modification of titanium oxide [36]. Although commercial applications of lead-based materials surpassed it, renewed interest has been sparked for BT-based piezoelectric and ferroelectric materials [4] in light of environmental concerns and new policy directions (RoHS, WEEE).

In addition to that, barium titanate also exhibits a complex temperature dependence of the dielectric permittivity with anomalously high values ($\varepsilon = 6000$), with its maximum occurring at the same temperature of a structural phase transition [37]. Barium titanate crystallizes in the

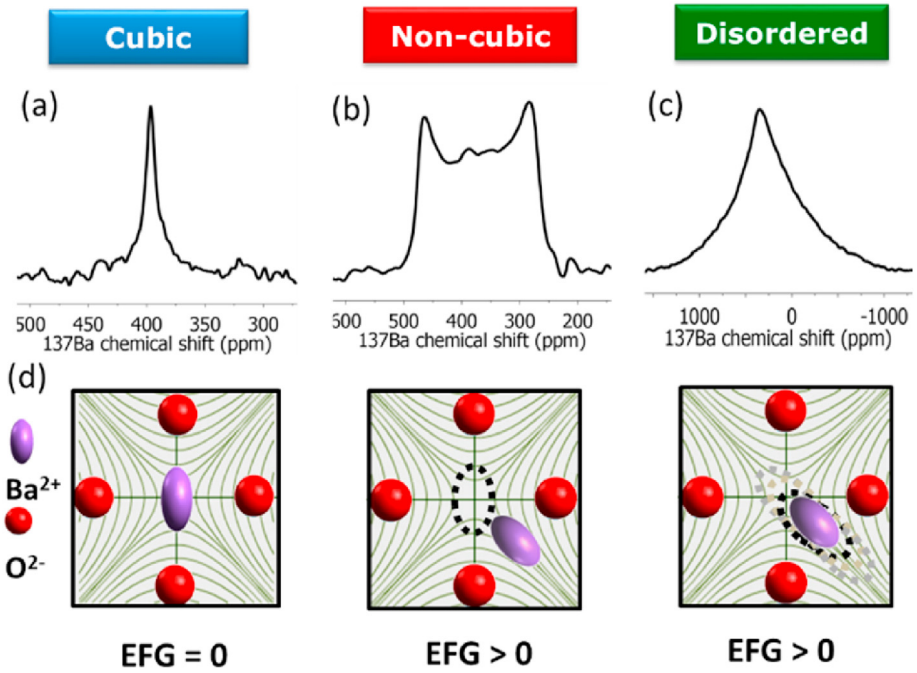

Fig. 4. ^{137}Ba NMR spectra of $BaTiO_3$ in (a) cubic, (b) tetragonal polymorphs. (c) $BaTiO_3$-based solid solution. (d) Relation between local structure and EFG for the three cases above.

perovskite structure. The prototypical perovskite structure belongs to the space-group *Pm$\bar{3}$m*. Oxygen ions form a lattice similar to a face-centered cubic one, where one out of four oxygen ions is substituted by the A cation, forming the A-site. This 12-fold coordinated site has the shape of a dodecahedron and is occupied by Ba^{2+} in barium titanate. The B-site consists of the octahedral interstices and is occupied by the smaller B cation (i.e. Ti^{4+} for barium titanate).

For barium titanate, as for most perovskites, structural distortions are a function of the temperature upon cooling from sintering temperatures, resulting in a series of phase transitions for this material [38,39]. Since the tolerance factor of $BaTiO_3$ is slightly above the unit, its structure is stabilized by ionic displacements of Ti^{4+} relative to the oxygen lattice. The symmetry of the structure is determined by the direction of this cationic displacement. In the high-temperature phase, this compound exhibits the prototypical cubic Pm3*m* structure. With decreasing temperature, a transition into a tetragonal P4mm phase occurs around 120 °C with the elongation of the unit cell in the (100) direction [40]. Two other transitions also take place, one at 15 °C and another at −80 °C. The first results in an orthorhombic *Amm2* [41] structure, and the second results in a rhombohedral *R3m* [42] symmetry.

3.1.1. *Quadrupolar interaction in $BaTiO_3$*

These phase transitions have a profound impact on the local structure of the material and can be easily discerned with NMR spectroscopy. The ideal NMR-active nucleus in $BaTiO_3$ is ^{137}Ba. It is a quadrupolar nucleus, which means that the shape and width of its NMR spectra are dominated by the quadrupolar coupling. This is an interaction between the nucleus and the electric field gradient (EFG) generated by the neighbouring atoms, which results in broadening of the NMR lines. The electric field gradient on the site of a given nucleus is determined by the electric charge distribution surrounding it, which is generated by its own electrons and neighbouring ions. This tensor property is especially sensitive to the immediate vicinity of the nucleus, as it scales with r^{-3} [6,19].

^{137}Ba NMR spectra from different polymorphs of $BaTiO_3$ have been first investigated by Bastow and Whitfield [43]. The spectrum of the cubic polymorph displays a narrow line (Fig. 4a), which reflects the cubic local symmetry around Ba^{2+} cations and a vanishing EFG above the Curie temperature. Contrastingly, the tetragonal polymorph exhibits a broader

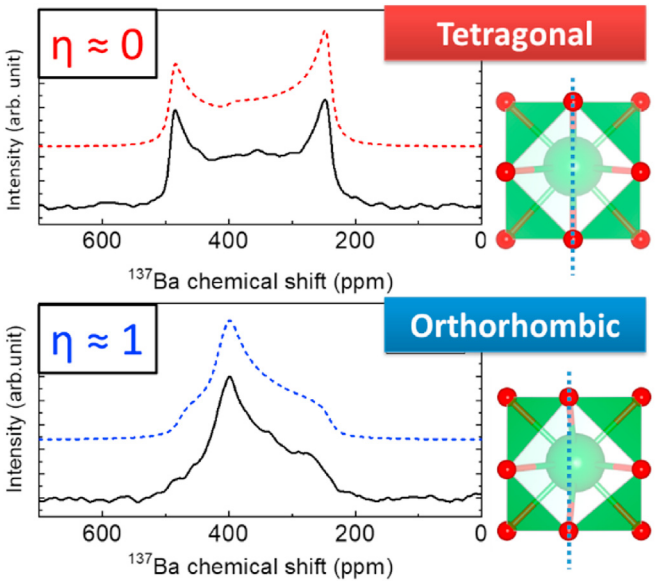

Fig. 5. Experimental and simulated ^{137}Ba NMR spectra for the P4mm and Amm2 polymorphs of $BaTiO_3$. Vertical dashed line in structure models represents a symmetry rotation axis.

line with two distinct maxima at its edges (Figs. 4b and 5 top). This shape is consequence of the orientation dependence of the quadrupolar interaction, and reflects the axial symmetry of the EFG tensor for a sample with an isotropic distribution of crystallites (i.e. a powder or ceramic sample). The width of the spectrum is a direct measure of the magnitude of the main component (V_{zz}) of the EFG tensor (analogous to Z^{PAS} in Fig. 3a) on the nuclear site, translated in terms of the quadrupolar coupling constant (C_Q). The value of C_Q follows the temperature dependence of the electric polarization, mirroring the structural origin of this property [44], and amounts to C_Q = 2.8 MHz close to room temperature.

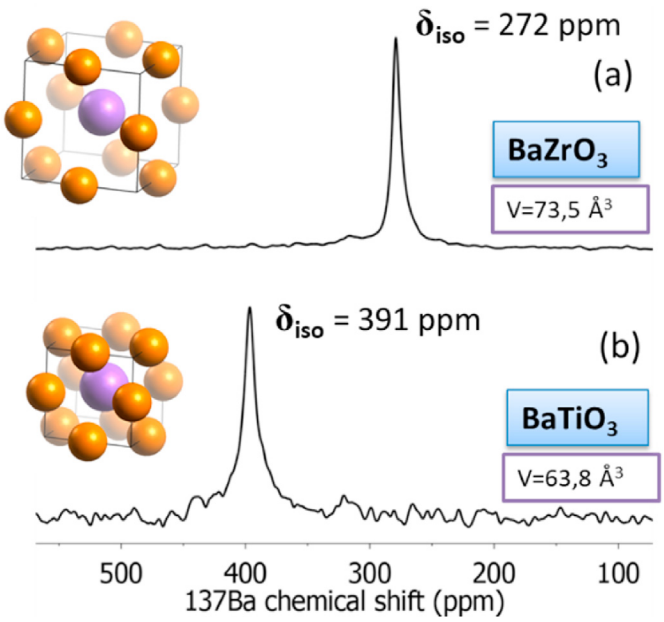

Fig. 6. ^{137}Ba NMR of (a) $BaZrO_3$ at room-temperature (b) $BaTiO_3$ above its Curie temperature.

Further cooling results in a transition into the orthorhombic polymorph, with significant change in the shape of the ^{137}Ba NMR spectrum. Fig. 5 contrasts the ^{137}Ba NMR lines for the tetragonal P4mm and orthorhombic Amm2 polymorphs of $BaTiO_3$ [43]. Despite their similar width, the latter displays a single maximum close to the centre of the line, flanked by shoulders on the edges. This specific shape is consequence of a decrease in the local symmetry of the A-site for the Amm2 polymorph, for which the ^{137}Ba nucleus is not located along a rotation symmetry axis (Fig. 5). The different shape these spectra exhibit is consequence of the point symmetry of the local environment of Ba^{2+} cations and how it influences the EFG in each polymorph.

In detail, while for the tetragonal phase (T) the barium site exhibits an axial symmetry (rotation axis about the c axis), in the orthorhombic phase (O) it exhibits a non-axial symmetry. This fact results in an asymmetry parameter (η) equal to 0 for the T phase and approximately 1 for the O phase. In terms of the EFG tensor, this non-axial symmetric environment results in different values for its V_{xx} and V_{yy} components (different than Fig. 3a, which depicts an axial symmetric tensor with $X^{PAS} = Y^{PAS}$). This difference is quantified by the asymmetry parameter η, which value can vary between $\eta = 0$ (axial symmetric), $0 < \eta < 1$ (non-axial symmetric) and $\eta = 1$ (C_∞) [45]. This property of ^{137}Ba NMR lines allows one to readily determine whether a $BaTiO_3$ sample exhibits the T or O polymorph.

3.1.2. ^{137}Ba chemical shift in perovskites

Besides the width and shape of the NMR line, its position also entails valuable information about the local structure of a given ion, such as coordination number, average bond length and the chemical nature of neighbours and next-near neighbours. The position of an NMR signal can be expressed either in terms of frequency, or more commonly as a frequency shift measured from the line position of a reference compound. The latter is called the chemical shift and has a dimensionless unit of ppm (parts per million), with respect to the absolute Larmor frequency of the probed nucleus in the reference compound. The standard reference for ^{137}Ba is a 1 M aqueous solution of $BaCl_2$, with a resonance at 0 ppm.

The chemical shift is an NMR parameter intimately connected to the electron density surrounding the nucleus, and consequently, is sensitive to the chemical bonding and its effects on the probed atom. A bare nucleus would exhibit a higher NMR frequency (i.e. shifted to the left of the spectrum) than one surrounded by electrons, as these shield the nucleus from the equipment's magnetic field (B_0). Hence, they lower the value for the effective, local, magnetic field (B_{loc}) that interacts with the probed nucleus and is responsible for its NMR frequency, and ultimately, line position. For a higher frequency and chemical shift one speaks of a deshielded environment in NMR jargon.

The chemical shift interaction is also described by a tensor (Fig. 3a), in an analogous manner as for the quadrupolar interaction. However, effects from the anisotropy of the chemical shielding (CSA) are either often small for a rather ionic environment, such as those found for most cations in oxides, or eclipsed by the larger quadrupolar interaction. Despite that, the CSA has an observable effect in $BaTiO_3$ for ^{47,49}Ti NMR [46], it has a major role in determining the spectra of ^{17}O NMR [47] and reflects the symmetry around O^{2-} sites, as well as in ^{207}Pb NMR [48] of oxides and its relation to a covalent or ionic character of the local environment of Pb^{2+} [49].

The first report about the chemical shift of ^{137}Ba NMR in perovskite oxides compared the line position for $BaZrO_3$, $BaTiO_3$ and BaO [50]. $BaZrO_3$ has a cubic structure at room temperature. Due to the absence of the quadrupolar interaction its spectrum consists of a single, sharp peak (Fig. 6a), from which the value of the chemical shift can be directly read as the position of peak's maximum at 272 ppm. The same procedure can be performed for $BaTiO_3$ above the Curie, with a chemical shift of 391 ppm (Fig. 6b). This value is also observed for the tetragonal polymorph. However, an accurate determination of the chemical shift in the presence of the quadrupolar interaction requires simulation of the spectrum to account for both interactions and extract the NMR parameters from experimental data.

The different values of chemical shift between $BaZrO_3$ and $BaTiO_3$ reflect the difference in the local environment of Ba^{2+} cations in both materials. In a simplistic interpretation, the higher ^{137}Ba NMR frequency for cubic $BaTiO_3$ indicates a lower electron density surrounding the probed nucleus. This may be attributed to the shorter Ba–O distances in this structure when compared to $BaZrO_3$. Oxygen is a very electronegative bonding partner, its proximity to a cation can deshield it by effectively withdrawing electron density, with an consequent shift the NMR signal to higher frequencies.

Alternatively, the different bonding character and polarizability of the next-near neighbour (Zr^{4+} v. s. Ti^{4+}) should also influence the electron density on the barium site and, hence, have influence on the chemical shift of these compounds. Furthermore, the coordination number (CN) may also have a considerable influence on the chemical shift. BaO (CN = 6) exhibits a chemical shift of 753 ppm [50], a much higher value in comparison to its perovskite counterparts (CN = 12). This fact can be explained by the fewer number of surrounding oxygen atoms [51], which are located much closer to barium cation in BaO and can more effectively withdraw electron density from this cation in the rock-salt structure.

However these empirical relations of the chemical shift might be appealing to understand in terms of a single structural parameter, a precise correspondence between the chemical shift and structural models can only be provided by quantum chemical computations (e.g. DFT) that calculate the local current induced by the external magnetic field on the position of the probed nucleus due to surrounding electrons [27,28].

3.1.3. ^{137}Ba NMR – effect of disorder

Despite the remarkable dielectric properties that barium titanate displays, pure ceramics present a very narrow temperature range where the permittivity peaks [38]. Such strong temperature dependence might be undesired for applications where temperature variation is expected. In addition to that, the range of the Curie temperature of pure barium titanate may not necessarily match the required operation temperature. During the research effort that resulted in barium titanate [37], it was soon recognized that impurities, or so-called additives, have a significant influence on the material's electrical properties. Due to the capability of the perovskite structure to host different kinds of atoms simultaneously, additives can be added in 1–20% weight, forming solid solutions between

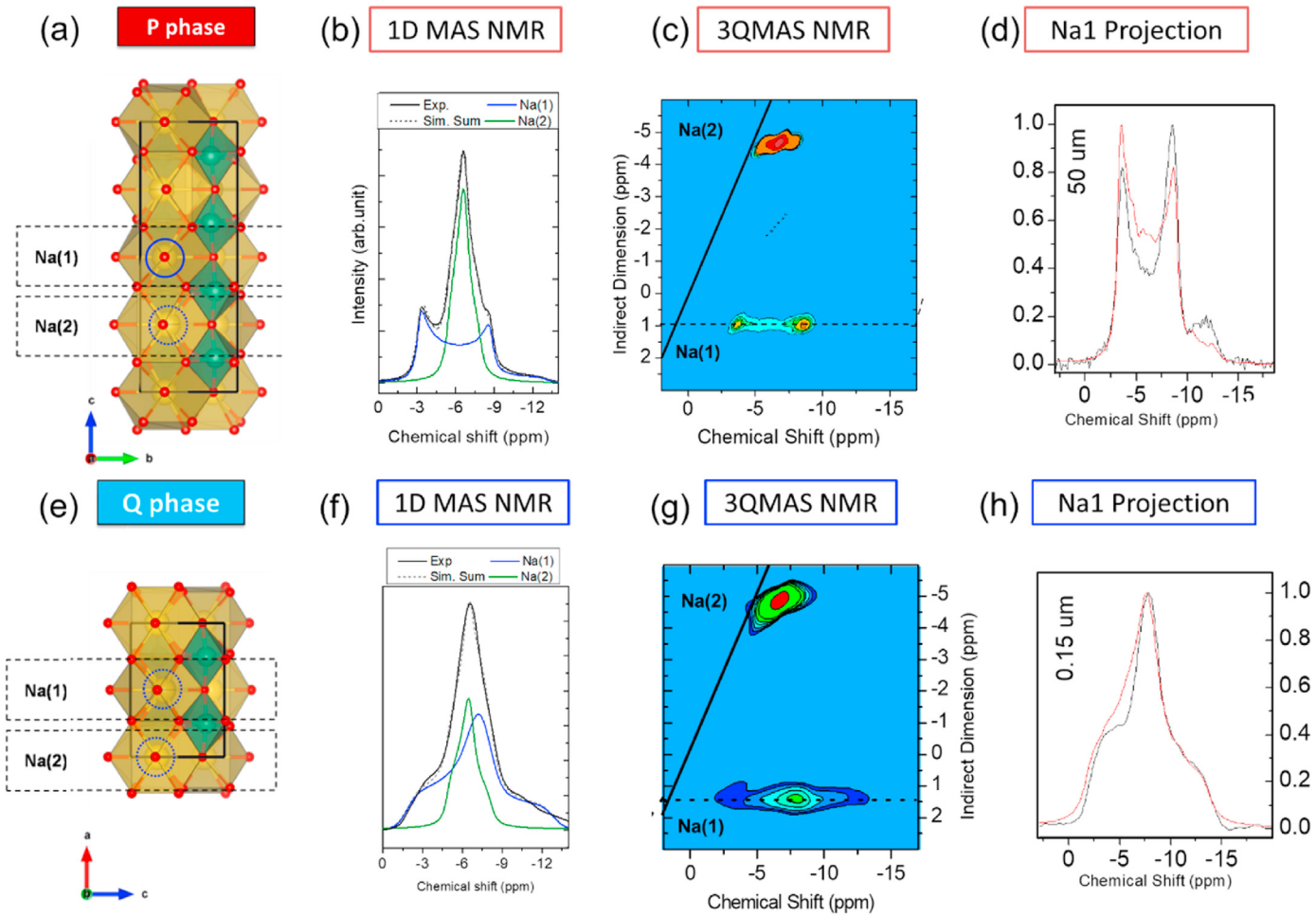

Fig. 7. Unit cell of $NaNbO_3$ and ^{23}Na NMR spectra thereof. (a–d) P phase and (e–h) Q phase.

the chemical modifier and barium titanate. One example is the substitution of the A-site with Sr^{2+}, that shifts Tc towards lower temperatures [52].

In addition to engineering electrical properties of a material, doping and formation of solid-solutions has a significant impact on the structure, mainly in terms of structural disorder, which are challenging to grasp with conventional characterization techniques employed in ceramics research. NMR spectroscopy may play an important role in understanding the local structure disorder caused by chemical modifiers and help to relate this information to the tuned electrical properties.

Gervais et al. [53] studied the formation of $Ba_{1-x}Sr_xTiO_3$ solid-solutions across the complete phase diagram and analysed the effect of Sr^{2+} content on the local structure of Ba^{2+} by means of ^{137}Ba NMR spectroscopy. Contrasting to the well-defined line shape for tetragonal $BaTiO_3$ with two maxima, an increase in strontium content results in a smearing out of sharp features of the line shape. From $x \geq 0.2$, a featureless, asymmetric lineshape is observed, with a pronounced tail towards lower frequencies, as depicted in Fig. 4c. This shape is characteristic for a distribution of quadrupolar coupling constants [54] and is attributed to the broad variation of distortions for the Ba site, due to the random distribution of Sr atoms across the lattice.

If one is interested in quantifying the magnitude of local structure disorder, simulation of NMR spectra can be performed as a superposition of lines with varying NMR parameters. For the case of $Ba_{1-x}Sr_xTiO_3$ and perovskite solid-solutions alike, a well-defined breaking of the average symmetry can be detected with diffraction techniques. Therefore, one may assume that the Ba local structure remains axial symmetric and the distribution of structural distortions and ionic displacements can be grasped by a Gaussian distribution of C_Q constants only (Fig. 4c). Using this approach, it was found that the magnitude of local structure distortion increases with increasing Sr content, despite the observation of an average cubic symmetry for $x \geq 0.2$ in diffraction data [53]. This is a prime example of how divergent the average and local structure of perovskites can be.

In case a higher degree of structural disorder should be considered, where the totality of the local environment can no longer be regarded as axial symmetric, a distribution of all components of the EFG tensor is necessary. Due to the fact that this is a traceless tensor, some restrictions apply, which have been considered in great detail by the model of Czejzek [55] for the distribution of EFG in glasses, and its extension by Le Caër [56], which attempts to retrieve information about the local structural disorder from the distribution of NMR parameters.

3.2. *$NaNbO_3$-based perovskites*

Besides titanates, niobates are also considered as lead-free alternatives in piezoelectric applications. $NaNbO_3$ is namely an end member of several alkaline niobate-based solid solutions, such as $(K_x,Na_{1-x})NbO_3$ or $(Li_x,Na_{1-x})NbO_3$ and their modifications, which represent an important group of environmentally-friendly lead-free piezoceramics [57,58]. More recently, interest in the antiferroelectricity of $NaNbO_3$-based materials [59,60] has grown due to their potential use as electroceramics in high-energy density capacitors [61,62], which are required for example in AC/DC inverters for electric vehicles and the integration of renewable power generation in the electrical grid.

Sodium niobate ($NaNbO_3$) was first developed by Matthias in 1949 [63]and has since drawn attention due to its physical properties and

complex structure, as it undergoes six phase transitions from the low temperature polymorph up to the cubic aristotype. The crystal structure of these seven polymorphs were determined in the 1960s and 1970s and summarized by Megaw in 1974 [64]. At room temperature, $NaNbO_3$ exhibits a non-polar, antiferroelectric polymorph with Pbcm space group (P phase), and a polar, ferroelectric polymorph with $P2_1ma$ space group (Q phase).

The P phase shows a quadrupled super cell with respect to the aristotype perovskite (Fig. 7a), due to its specific tilting system [65]. It displays two sodium positions in the A-site with very distinct local structures, with site Na1 displaying shorter Na–O and a smaller volume for the NaO_{12} cage than site Na2. It is also interesting to note that Na1 is more distorted than Na2. A further difference with respect to their local symmetry is the fact that Na1 is poised on a symmetry rotation axis, whereas Na2 is found in a non-axial symmetric environment, as this sodium atom is shifted away from the centre of the NaO_{12} cuboctahedron.

While the Q polymorph shares many similarities with the P phase, it exhibits a less intricate tilt system, which results in a doubling of the elementary unit cell of the perovskite structure (Fig. 7e). As far as the local structure of sodium sites is concerned, the main difference between the P and Q phases is the breaking of axial symmetry for Na1 in the latter, a feature easily detectable with NMR spectroscopy. All these characteristics of both room-temperature polymorphs of $NaNbO_3$ are reflected in their ^{23}Na NMR spectra.

3.2.1. ^{23}Na NMR spectroscopy

The element sodium has a single natural isotope, ^{23}Na. This nucleus has a magnetic moment with a spin number equal to 3/2 and a gyromagnetic ratio of 7.0761 10^7 rad T^{-1} s^{-1} [7], which amounts to about one fourth of the gyromagnetic ratio of ^{1}H. Together with a natural abundance of 100%, this property makes ^{23}Na a very sensitive nucleus for the NMR experiment. This nucleus also bears a quadrupolar electric moment of 0.104 barn [8], what makes sodium nuclei sensitive to electric field gradients (EFG) imposed by their surroundings. These characteristics, together with its ubiquitous presence in inorganic materials, make ^{23}Na an ideal probe for the investigation of the local structure of solids by means of solid-state NMR.

NMR spectroscopic research of this nucleus started more than half a century ago with the investigation of sodium salts. The very first NMR spectrum of ferroelectric sodium nitrite ($NaNO_2$) has been recorded in 1960 by Alarich Weiss [66] and a correlation between the magnitude between quadrupolar coupling constant (C_Q) and the symmetry of the arrangement of neighbouring atoms was found, with increasing C_Q values as the point symmetry of the sodium site further deviates from a cubic one [67].

The reference and zero point for the chemical shift scale of ^{23}Na is $NaCl_{(aq)}$ 0.1 M [68]. Nonetheless, older literature often cites $NaCl_{(s)}$ as the zero point of the scale, whose resonance appears +7.2 ppm to that of sodium chloride in aqueous solution. The chemical shift values for sodium in non-conducting solids range from +20 ppm to −25 ppm, and its physical meaning in the solid-state has been mainly attributed to the proximity, nature and number of neighbouring atoms and, to a lesser extent, to next-nearest-neighbours [67]. From the investigation of the chemical shift of ^{23}Na in silicates, it has been recognized that this spectroscopic parameter is mainly influenced by the average length of the Na–O bonds surrounding this nucleus [67,69–71]. A linear correlation between the chemical shift of ^{23}Na and the average Na–O distance was reported for crystalline silicates. A similar approach has been applied to alumina-silicates, for which a linear relationship between the chemical shift and the <Na–O> average distance has also been found, albeit with different function coefficients, which account for coordination number and next-nearest-neighbour effects [70,72].

3.2.2. ^{23}Na NMR of $NaNbO_3$

The ^{23}Na MAS NMR spectrum of the P phase is depicted in Fig. 7b, along with a simulation of the lines for each sodium site. A comparison of their line shape reveals important aspects of their individual local structure. The signal for Na1 is broader than the signal of Na2, and reflects the larger distortion of the NaO_{12} cage of the former (Fig. 7a). This distortion results in a large EFG on the Na1 site, which can be quantified in terms of the quadrupolar coupling constant (C_Q). Furthermore, the signals of both sodium sites differ in their shape, a trait that reflects the local symmetry. While two maxima are observed for the signal of Na1, a shape characteristic of an axial-symmetric environment, a single maximum is present in the signal of Na2, which reflects the fact that this sodium atom is shifted away from a rotation axis of symmetry, as expected from its position away from the centre of the NaO_{12} cuboectahedron.

The ^{23}Na NMR parameters for the P phase of $NaNbO_3$ can be summarized as the following: Na (1) site with an axially symmetric environment (Na (1): $C_Q = 2.1 \pm 0.1$ MHz, $\eta = 0.0 \pm 0.1$, $\delta_{iso} = -1.0$ ppm) and Na (2) site with a smaller quadrupolar coupling constant and non-axial symmetry (Na (2):$C_Q = 1.0 \pm 0.1$ MHz, $\eta = 0.9 \pm 0.2$, $\delta_{iso} = -5.0$ ppm) [73]. The isotropic value of the chemical shift (δ_{iso}) can be determined in this experiment without contribution of second order shift from the quadrupolar interaction, with the different values observed for each sodium site being related to average Na–O distance [69].

The same characteristics are observed in the two-dimensional 3QMAS (also called MQMAS) spectrum (Fig. 7c), which resolves both sites in a bird's-eye view fashion, by disentangling the contribution of the chemical shift and the quadrupolar interaction to line position in the spectrum. This technique allows the analysis of projections from individual signals (Fig. 7d), which provides a further tool for the accurate determination of NMR parameters by simulation of spectra.

The different tilt systems for the P and Q phases of $NaNbO_3$ have the most impact on the local structure of the Na1 [74], and result in breaking of the axial local symmetry for this particular lattice position (Fig. 7e). The resulting differences in line shape are clear (Fig. 7f), as the Na1 line now exhibits a single maximum flanked by two shoulders instead of the characteristic shape observed for the Na1 site in the P phase. Regardless of the fact that both sodium sites display non-axial symmetry in the Q phase, they still can be easily distinguished by the magnitude of local structure distortion, which remains similar as for the P phase. These differences between the *P* and the *Q* polymorphs can be summarized by the asymmetry parameter (η) of site Na (1) changes drastically from 0 to 0.9 ± 0.2, while the value of C_Q remains constant [73]. The distinct line shapes can be more easily contrasted by the analysis of the 3QMAS spectrum of the Q phase (Fig. 7g) an its projection for the Na1 site (Fig. 7h), which resemble the comparison between the ^{137}Ba NMR spectra of the tetragonal and orthorhombic polymorphs of $BaTiO_3$ (Fig. 5), albeit now under MAS.

3.2.3. Applications of NMR to $NaNbO_3$

The first NMR study of $NaNbO_3$ was performed by Wolf et al. in 1979, and revealed important characteristics about its phase transitions and the role of octahedral tilting and tilting dynamics, but could not resolve local structural characteristics of specific sites [75]. Later development of fast sample rotation (MAS) and the advent of two-dimensional MQMAS pulse sequence [29] allowed for high-resolution of NMR spectroscopy of quadrupolar nuclei. Ashbrook et al. employed this technique to analyse the structure of $NaNbO_3$ and found evidence for coexistence of two $NaNbO_3$ phases in samples from hydrothermal synthesis [69]. Subsequent work by Johnston et al. used a combination of ^{23}Na NMR, DFT calculations and neutron diffraction to clarify the nature of this secondary phase as the Q phase, which is found along the P phase in samples prepared with different synthesis methods [73]. Interestingly, an ^{93}Nb NMR investigation of these samples revealed a very similar local environment for the B-site, regardless of the $NaNbO_3$ phase investigated [76].

Koruza & Groszewicz et al. [77] investigated the grain-size dependence for the occurrence of either P and Q phases of $NaNbO_3$. ^{23}Na MQMAS NMR was employed to study sintered ceramic samples with an average grain size ranging from 150 nm (pure Q phase) to 50 μm (pure P

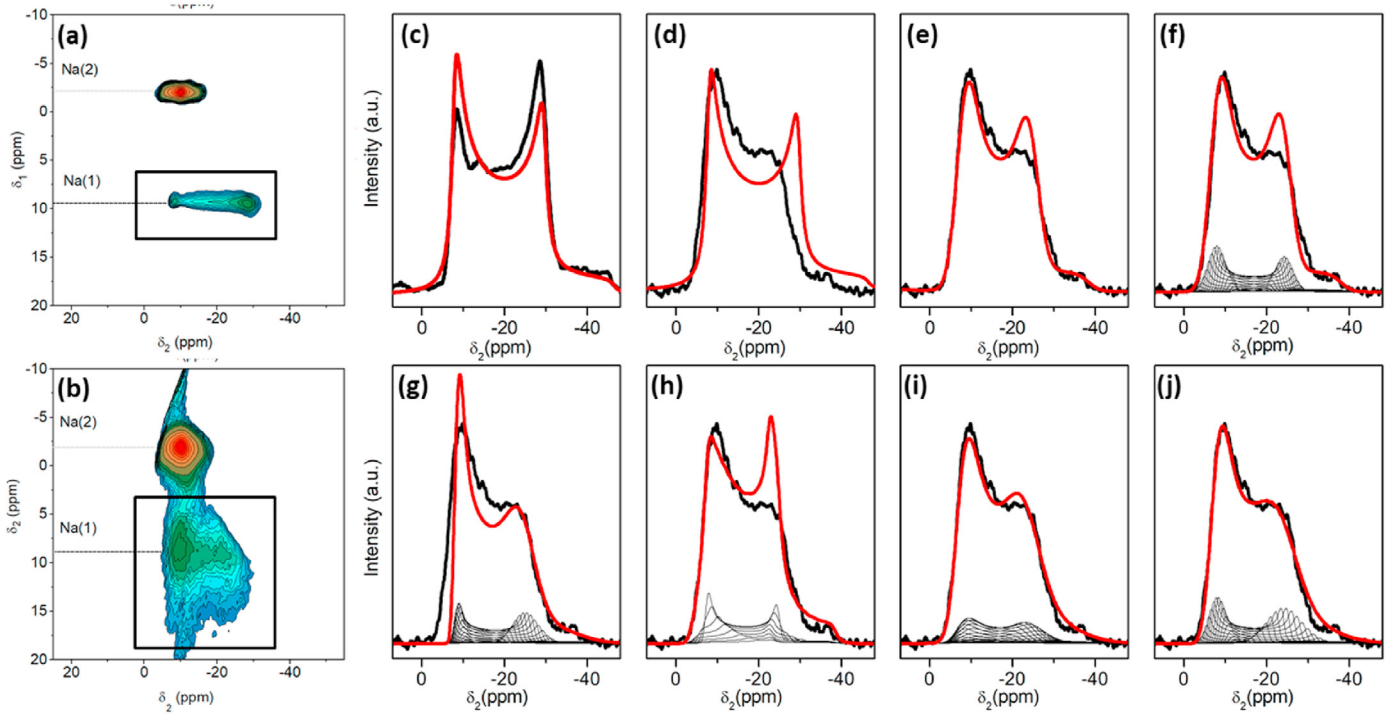

Fig. 8. ^{23}Na STMAS NMR spectra of (a) $NaNbO_3$ and (b) $0.95NaNbO_3$-$0.05SrSnO_3$ solid solution. (c) projection of Na1 signal for pure $NaNbO_3$. (d–j) Simulations for the Na1 projection for this solid solution (see text for details).

phase). Although this technique offers high resolution between the signals from Na1 and Na2 sites, the Na1 sites of the P and Q phases overlap in the two-dimensional spectra. By simulating the line shape of the overlapped Na1 signal as a combination of powder patterns characteristic of this sodium site in the P and Q phases (Fig. 7d and h, respectively), it was possible to quantify their relative amount. Based on this information and the distribution of grain sizes, a critical grain size of 0.270 μm was found, below which the Q phase is stabilized.

Egert at al. [78] improved the resolution between ^{23}Na signals of different $NaNbO_3$ polymorphs by the application of STMAS NMR, a two-dimensional pulse sequence closely related to MQMAS. Despite the more stringent experimental calibration requirements, especially for setting the magic angle accurately and on stable spinning of ceramic samples, STMAS offers the advantage that Na1 signals from P and Q phases are resolved in the 2D spectra. This trait allows a more precise quantification of phases by simple integration of signal area, which relinquishes from any assumption for the exact line shape of each signal and distortions thereof due to non-ideal probe response. This technique played a pivotal role in the characterization of electric-field induced stabilization of the Q polymorph, studied in more detail by Zhang et al. [79].

The stabilization of the Q polymorph and the improvement of energy storage capabilities can also be achieved by the chemical modification of parent $NaNbO_3$, as demonstrated previously by Shimizu et al. [74] In a more recent work by Koruza et al. the design of new $NaNbO_3$ ferroelectrics guided by DFT calculations has been proposed [80]. This publication reports on solid solutions between $NaNbO_3$ and $SrSnO_3$ as a viable way to improve energy storage density, and describes a detailed characterization of the underlying structure, with particular attention to the local structure from the point of view of NMR spectroscopy.

Building up on the current understanding about pure $NaNbO_3$ (Fig. 8a,c), the authors employed ^{23}Na STMAS NMR to analyse the local structure changes caused by the formation of solid solutions with $SrSnO_3$ (Fig. 8b,d), and concluded that it results in a less distorted, albeit more disordered local environment for the Na1 site. In detail, the broader signals in the STMAS spectrum of (1-x)$NaNbO_3$- (x)$SrSnO_3$ with $x = 0.05$ are a consequence of local structure disorder by the shared lattice occupation with Sr^{2+} and Sn^{4+}. Both sodium sites still maintain NMR parameters characteristic of the P phase, whereas the width of Na1 signal decreases for the solid solution. This change is translated into a smaller C_Q value of 1.90 MHz and indicates a less distorted local structure (Fig. 8d).

Furthermore, Na1 displays more intense signal smearing than Na2 when compared to pure $NaNbO_3$. Different than other perovskite solid solutions, where the distribution of local structure parameters results in a featureless line shape, the Na1 projection for (1-x)$NaNbO_3$- (x)$SrSnO_3$ with $x = 0.05$ develops only a smearing of its maxima. Interestingly, the right-hand maximum is much less pronounced than the left side, which raises questions about the actual distribution of NMR parameters (Fig. 8d-j).

This situation offers an interesting example to illustrate the effect of distribution of individual NMR parameters on the line shape of quadrupolar nuclei. The experimental projection cannot be reproduced either by a broader window function (Fig. 8e) or a Gaussian distribution of chemical shift (Fig. 8f). A distribution of asymmetry parameters (Fig. 8h) has the opposite effect and makes the right-hand side more pronounced. Contrastingly, a narrow distribution of C_Q parameters attenuates the right-hand maximum (Fig. 8g). In combination with a distribution of chemical shift (Fig. 8i), the right-hand side is flattened, and finally reproduces the experimental line shape when a correlation between chemical shift and C_Q values is considered (Fig. 8j). This distribution amounts to an average CQ of 1.9 (0) MHz and an average chemical shift of −2 (8) ppm, with a distribution width (i.e., standard deviation of a Gaussian distribution). of 0.13 (0) MHz and 1.(2) ppm, respectively. These values are in accordance with numbers expected from DFT calculations of NMR parameters in disordered structural models in terms of tilting of octahedral and average Na–O distances [80]. This analysis supports a more disordered, yet less distorted local environment for sodium site Na1 as advantageous for the stabilization of the AFE phase.

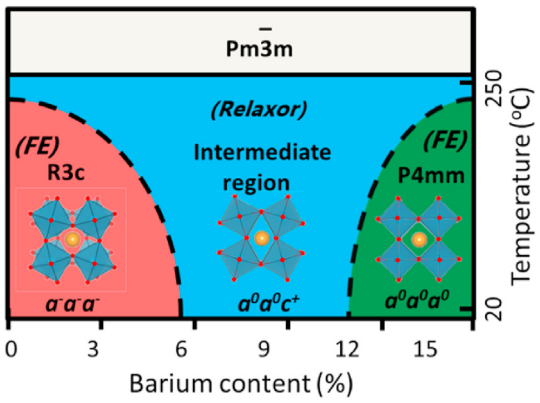

Fig. 9. Illustrative phase diagram for (100-x) $(Na_{1/2},Bi_{1/2})TiO_3$-x $BaTiO_3$.

3.3. NBT-based perovskites

Besides $BaTiO_3$ and $NaNbO_3$-based materials, $(Na_{1/2},Bi_{1/2})TiO_3$-based materials constitute the third family of lead-free piezoelectric ceramics [2,81,82], and are currently also considered as oxide ion conductors [83]. NBT and its solid solutions have attracted much interest as a promising lead-free piezoelectric material, not only from an environmental point of view, but also due to the high piezoelectric coefficient it exhibits when doped with barium (NBT-xBT), for which optimum properties arise at a barium content around 6% [84,85]. However, in order to achieve technical readiness, detailed knowledge of the structure is fundamental. In spite of that, there is still much disagreement over the phase diagram of NBT-xBT (Fig. 9).

It is well accepted that the phase diagram of NBT-xBT consists of a region of rhombohedral (*R3c*) symmetry which is separated from a tetragonal (*P4mm*) region by a boundary around a barium content of 6% [82]. However, the structure of compositions found in this region of the phase diagram is still a controversial issue. Although the first account on this boundary, by Takenaka, suggests this separation is a morphotropic phase boundary (MPB) [85], subsequent publications report on it as another region in the phase diagram, rather than a boundary. The macroscopic structure of compositions located between the rhombohedral and tetragonal regions has been reported by several authors, albeit with different average symmetries, which ranged from rhombohedral (*R3m*) [86], tetragonal (*P4bm*) [87] and even cubic [88]. Furthermore, the complexity of the structure of NBT and its barium doped versions has been often described by the coexistence of two different tilt systems. As an example, the coexistence between $a^-a^-a^-$ and $a^-a^-c^+$ tilt systems has been reported for pure NBT [89]. In addition to that, the coexistence of $a^-a^-a^-$ and $a^0a^0c^+$ tilt systems has been reported for MPB compositions (e.g. NBT-6BT) [90].

Each of these studies [85–90] is consistent and well justified when looked upon individually, but when regarded in the big picture they are found to be in direct contradiction with each other. This disagreement may have its origin on the very slight structural distortions that are present in these intrinsically disordered materials, which result in a structure very close to the ideal perovskite and pose a challenge for the conclusive determination of their symmetry. Furthermore, many compositions of the NBT-xBT series are found in a relaxor state [90,91], a state marked by the presence of polar nanoregions (PNR), for which structural distortions exhibit very short coherence length of only a few unit cells. As a consequence, techniques sensitive to the macroscopic structure might oversee some crucial structural features present at the local scale.

Further understanding about these questions can be provided by the use of NMR spectroscopy. Although the characterization of ^{209}Bi NMR is very challenging, ^{23}Na is an amenable NMR-active nucleus that can reflect the local-structural traits of the A-site in these disordered perovskites based on NBT. Despite not quite as trivial, $^{47,49}Ti$ can also provide local structure information from the B-site perspective in these materials.

The first report of ^{23}Na NMR spectra for NBT by Aleksandrova et al. suggested the coexistence of different symmetries in single-crystal specimen [92]. This was followed by Groszewicz et al. with an *ex situ* ^{23}Na

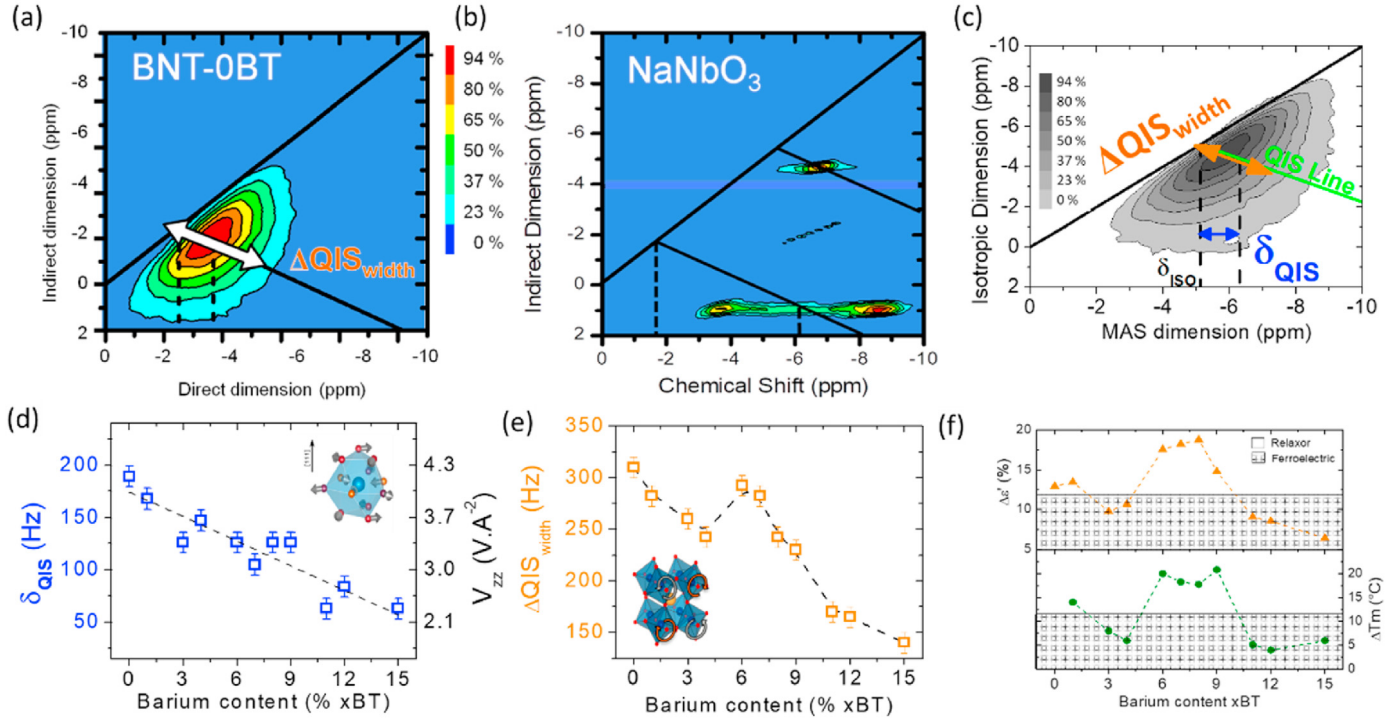

Fig. 10. ^{23}Na 3QMAS spectra of (a) NBT, (b) $NaNbO_3$ and (c) NBT-6BT. Structure-relevant NMR parameters extracted from 2D spectra, related to (d) magnitude of local structure distortion and (e) extent of local structure disorder, plotted as a function of barium content. (f) Frequency dispersion parameters from dielectric permittivity of NBT-xBT, characteristic of either a relaxor or ferroelectric state.

MAS NMR investigation about electric poling and the coexistence of cubic and non-cubic local symmetries in NBT-xBT ceramics found in a relaxor state [93]. In a further work, details of the structural disorder as a function of barium content, its relation to the relaxor state and the role played by tilting disorder for this state were investigated with ^{23}Na 3QMAS NMR [94]. This conclusion was further supported by a ^{47,49}Ti NMR study that showed the B-site local environment to remain constant for NBT-xBT compositions despite different tilt systems [95]. In a more recent work, a combination of ^{27}Al NMR and DFT calculations was applied to explore the action of acceptor doping in the structure of Al-doped NBT and NKBT-BA solid solutions, revealing the full range of possible local environment for this cation in the perovskite structure [96]. Each of these works will be described in more detail in the following section; together they give a comprehensive status on the current understanding of the local structure of NBT-based materials and its relation to functional properties.

3.3.1. ^{23}Na NMR local structure disorder in NBT-xBT [94]

Two-dimensional ^{23}Na 3QMAS NMR experiments enabled the study of the quadrupolar interaction in lead-free electrically functional ceramics of the series NBT-xBT (Fig. 10a,c). They exhibit broad spectra with featureless shape, characteristic of local structure disorder. This shape contrasts to the one from a well-defined local environment, such as found in $NaNbO_3$ (Fig. 10b). These experiments allowed insight into a spectroscopic parameter related to the local structural, namely, the electric field gradient (EFG) at the sodium site. The shape of NMR signals indicates the local structure deviates from the average one, in that a variety of local structural motifs with significant local structure distortion is present. This diversity can be quantified in terms of a mean electric field gradient and its distribution width. These parameters are determined from the position and width of the 3QMAS signal (Fig. 10c), and are described in terms of the quadrupolar induced shift (δ_{QIS} - Fig. 10d) and the width along the QIS line (ΔQIS - Fig. 10e), respectively.

Furthermore, ^{23}Na 3QMAS NMR spectra of NBT-xBT as a function of barium content ($0 \leq xBT \leq 15$) demonstrate that both the mean EFG value and the EFG distribution width decrease upon barium addition to the structure [94]. While the mean value decreases monotonically (Fig. 10d), the width of the EFG distribution exhibits a peculiar composition dependence (Fig. 10e), with large ΔQIS values observed for compositions with very low (e.g. pure NBT) and intermediate (e.g. NBT-6BT) barium content. Interestingly, this composition dependence correlates strongly with the presence and intensity of frequency dispersion in dielectric spectra of NBT-xBT (Fig. 10f), a feature characteristic of the relaxor state [97]. This correlation raises the question about what structural features could be responsible for the observed composition dependence of the EFG and possibly bring one a step further towards a better understanding of the observed structure-property correlation.

Bearing these questions in mind, DFT calculations of EFG values for different structural models were performed. Different mechanisms of symmetry breaking were evaluated with respect to the role of barium addition on experimental EFG values and structure simulations. Three distortion mechanisms relevant to the perovskite structure were investigated with DFT calculations, namely: the effect of cation arrangement, polar cation displacements and octahedral tilting. The experimental trend of decreasing EFG values by addition of barium to the models was only reproduce when tilting was considered in the calculations.

Based on the outcome of these DFT calculations, it was inferred that the experimental EFG on sodium site reflects the behavior of octahedral tilting in NBT-xBT. These materials feature a continuous distribution of EFG values, which may be attributed to a continuous octahedral tilting disorder. This hypothesis contrasts to the established point of view in the literature. Although the octahedra tilting disorder in NBT-xBT is often explained by the coexistence of two well-defined tilt systems, which are observed when diffraction methods are applied, such a structure would result in two well-defined quadrupolar patterns for the NMR spectra; nonetheless, such a pattern is not observed, and a continuous distribution for the EFG is observed instead. This apparent disagreement may have its origin on the coherence length that each of these techniques is sensitive to.

Furthermore, the EFG distribution width correlated strongly with the spontaneous electric state of NBT-xBT. A broader distribution of EFG values, expressed as the ΔQIS parameter, is observed for compositions found in a relaxor state. Contrastingly, compositions that exhibit a spontaneous ferroelectric state display lower values of ΔQIS. This parameter can be understood as a measure of the degree of disorder in octahedra tilting. Hence, the correlation between ΔQIS and the dispersion of dielectric permittivity indicates that octahedral tilting disorder is a local structural feature concurrent with the occurrence of relaxor behavior in NBT-xBT materials [94].

3.3.2. ^{47,49}Ti NMR spectroscopy

Despite the natural occurrence of NMR-active isotopes, titanium NMR is not a widespread technique for the structural characterization of materials. The acquisition of NMR spectra of this element is challenging, mainly due to its very low sensitivity (Fig. 1). The low sensitivity of titanium NMR is a consequence of the low gyromagnetic constant and low natural abundance of its two active isotopes, ^{49}Ti (5.51%) and ^{47}Ti (7.28%) [7]. In addition to that, both isotopes are quadrupolar nuclei with relatively high spin quantum numbers (7/2 and 5/2) and strong quadrupolar moments (+0.24 (1) +0.302 (10) barn) [8]. Due to their similar gyromagnetic ratios (−1.5109 and −1.5105 10^7 rad T^{-1} s^{-1}) [7], both isotopes occur in same spectral region and are separated by only about 266 ppm [98]. This proximity is a further challenge, as both lines might overlap depending on the magnitude of the external magnetic and the electric field gradient on the titanium site.

These features of titanium NMR may account for the modest number of studies concerned with this technique. Among these, Padro et al. gives a very comprehensive NMR study of titanium in oxides [99], in which (Bi,Na)TiO_3 and $BaTiO_3$ are also covered. More specifically, ABO_3 materials with TiO_6 moieties resonate in the range between −850 ppm ($CaTiO_3$) and −690 ppm ($PbTiO_3$). Furthermore, a correlation has been reported between the mean Ti–O distances and the chemical shift [100]. The quadrupolar coupling constant (C_Q) and the electric field gradient (EFG) in these oxides also deliver information about the local structure, with the magnitude of displacement of titanium and the octahedral strain [100] as relevant features.

The reference compound for the chemical shift scale in ^{47,49}Ti NMR measurements is $TiCl_4$, which is liquid at room temperature [98]. Because of its very symmetric molecular geometry and rapid tumbling of molecules in the liquid state, this substance exhibits very sharp lines for both isotopes, a feature that counter weighs the low sensitivity of these nuclei. In spite of its high reactivity with air moisture, which produces hazardous $HCl_{(g)}$ and poses a risk to its use, the chemical shift scale is referenced with the ^{49}Ti resonance of neat $TiCl_4$(l) at 0 ppm. An alternative, secondary reference is $SrTiO_3$ [50], which in spite of being a solid, exhibits very narrow lines as consequence of its cubic structure (analogous to ^{137}Ba NMR of $BaZrO_3$ - Fig. 6a) and can be employed as a secondary reference. This fact can be attributed to its very symmetric local environment, which results in a negligible broadening due to 2nd order quadrupolar effects. Its ^{49}Ti resonance occurs at −843 ppm, and its width is a consequence of dipolar interactions only.

The measurement of titanium NMR spectra of samples with such narrow lines can be performed with simple one-pulse experiments. Conversely, the acquisition of broader lines requires the use of echo pulse sequences, which involve more pulses than the single-pulse sequence depicted in Fig. 2a. Anisotropic interactions between the nucleus and its local environment lead to a large broadening of NMR lines for solid-state powder samples. The broader the lines, the shorter the decay of the FID becomes. Consequently, a more significant share of the signal may be corrupted by pulse ring down or and other artifacts (e.g. acoustic ringing). Approaches to minimize these problems rely either on a spin echo or adequate phase cycling [101,102], but a trade-off with signal intensity or experiment times should be taken into account.

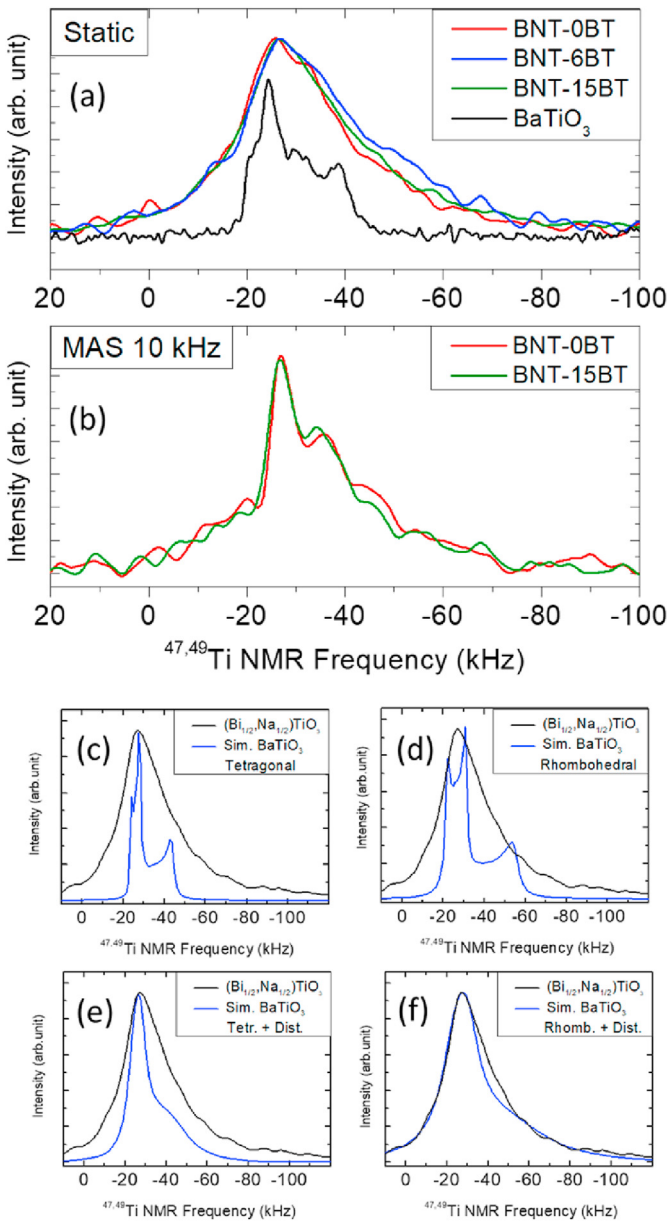

Fig. 11. ^{47,49}Ti NMR spectra of NBT-xBT. (a) static spectra, (b) MAS spectra, (c–f) simulations of the ^{47,49}Ti spectrum of NBT-0BT based on NMR parameters from different $BaTiO_3$ polymorphs.

3.3.3. *^{47,49}Ti NMR – B-site disorder in NBT-xBT [95]*

^{47,49}Ti NMR spectra of NBT-xBT samples with different barium content were investigated [95] (see Fig. 11). Three conclusions could be drawn based on the interpretation of these titanium spectra, which corroborate the interpretation of the ^{23}Na spectra and its relation to the structural features of NBT-xBT [94].

First, the local structure distortion around titanium nuclei is invariant to the chemical modification with barium across the MPB of NBT-xBT (Fig. 11a,b), a result which is in accordance to a previous investigation employing XAFS [103]. This fact implies that the action of barium in the structure is not directly related to the distortion of oxygen octahedra, which would directly impact the local environment around titanium nuclei, and, hence, their NMR spectra. Instead, the ^{47,49}Ti NMR spectra suggest the structural role of barium cations could be involved with how the oxygen octahedra units are arranged in space with respect to each other (i.e. in terms of octahedra tilting and tilt systems).

Second, the local structure around titanium nuclei is disordered. Spectra shape and its behavior under MAS indicate a distribution of both δ_{iso} and C_Q NMR parameters, which are representative of the chemical shift and quadrupolar interactions (Fig. 11c-f). These are closely related to the local environment of titanium, and could reflect the disorder present in the structure due to the random occupation of the A-site. Nevertheless, the B-site seems not to sense the fine tuning of structure disorder caused by the addition of barium, at least not as much as the A-site sodium. This fact further supports the hypothesis that the presence of barium cation does not lead to a distortion of the oxygen octahedra; instead it impacts the local environment of other A-site cation by tilting of TiO_6 octahedra. An analogous argument could explain the absence of changes in ^{93}Nb NMR spectra between the P and Q polymorphs of $NaNbO_3$ [76].

Third, a comparison between the ^{47,49}Ti NMR static spectrum of NBT-0BT to simulations based on NMR parameters from different $BaTiO_3$ polymorphs indicates the local symmetry for the B-site remains invariant. Whereas the line for pure NBT is much broader than for the tetragonal polymorph of $BaTiO_3$ (EFG $V_{zz} = 6.6$ V Å^{-2}), it matches quite remarkably the line width observed for its rhombohedral polymorph (EFG $V_{zz} = 9.4$ V Å^{-2}). Even the overall shape has a close resemblance when a Gaussian window function is added to the simulation to emulate the effect from distribution of NMR parameters due to local structure disorder. This procedure allows the estimation of the magnitude of the mean EFG value for the B-site in pure NBT and may be interpreted as a fingerprint of a rhombohedral distortion of its local structure.

3.3.4. *Coexistence of local symmetries in NBT-xBT [93]*

Besides the 3QMAS and the analysis of the central transition (CT), quadrupolar nuclei ($I \geq 1$) also exhibit additional 2I-1 transitions, the so-called satellite transitions [104]. The spinning sidebands envelope (SSE) of the satellite transitions in one-dimensional ^{23}Na MAS NMR spectra can also provide insight on characteristics of the quadrupolar coupling between this nucleus and the close surroundings of the A-site in NBT-xBT materials. The advantage of this spectral feature in comparison to the analysis of the central transition is the fact that the quadrupolar interaction of first order is the single interaction influencing its shape and width, without the contribution of the chemical shift [45,105].

By means of ^{23}Na solid-state NMR evidenced was provided for the coexistence of two local symmetries in the relaxor state of NBT-xBT materials, namely a cubic phase together with a non-cubic one [93]. Based on the relative area between spectral components attributed to the satellite and central transitions (i.e. the I_{SSE}/I_{CB}), the amount of cubic phase could be estimated for the unpoled, poled and depoled states of each investigated composition (Fig. 12). The cubic phase was found only for compositions that exhibit relaxor features in their permittivity curves, indicating the presence of this phase is intimately connected to relaxor behavior. It could also be shown that the electric field induced transition from a relaxor into a ferroelectric state is not only a reorientation of electric dipoles; instead, the cubic phase also becomes polarized. These results support a view of the microstructure of relaxors with PNRs embedded in a cubic non-polar matrix. Electric poling enables growth of PNRs, at expense of the matrix, and a ferroelectric state is achieved.

Annealing the poled samples and cooling them in a zero field resulted in the relaxor state again. The reappearance of the cubic phase at comparable amounts to the unpoled samples shows the reversibility of the poled state, and the relation between this cubic phase and the relaxor state. Furthermore, the shape of NMR spectra of poled samples suggests that the polar local structure is partially disordered. In addition to that, for barium contents below 6% that the local structure of the polar phase did not change due to the transition from a relaxor into a ferroelectric state, implying that the macroscopic structure of poled samples and the local structures of PNRs might be the same.

Permittivity curves for NBT-xBT ceramics have shown that electric field induced phase transitions are a common feature for relaxor compositions (Fig. 13), as evidenced by the presence of a ferroelectric state

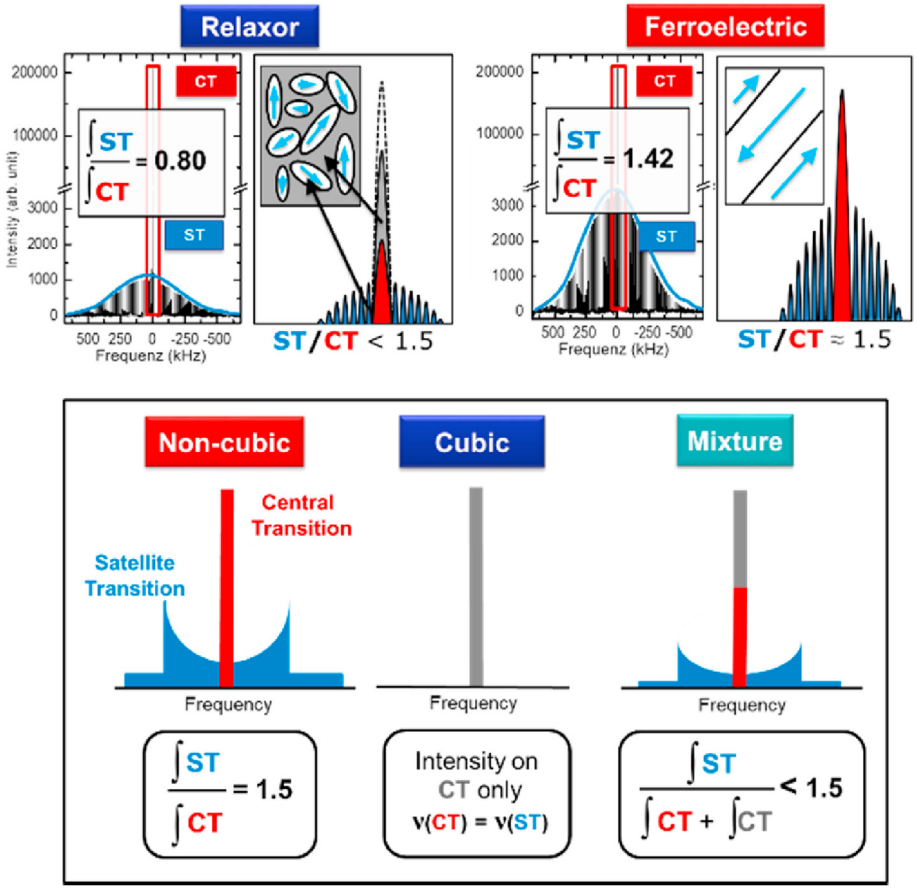

Fig. 12. Schematic ^{23}Na MAS NMR spectra of the satellite transitions (SEE) in NBT-xBT ceramic samples found in the relaxor and ferroelectric state. While the observation of SEE is evidence of presence of non-cubic symmetry, the analysis of the ratio between the area of the SEE and the centreband allows the quantification of a cubic content, whenever it deviates from the theoretical value of 1.5.

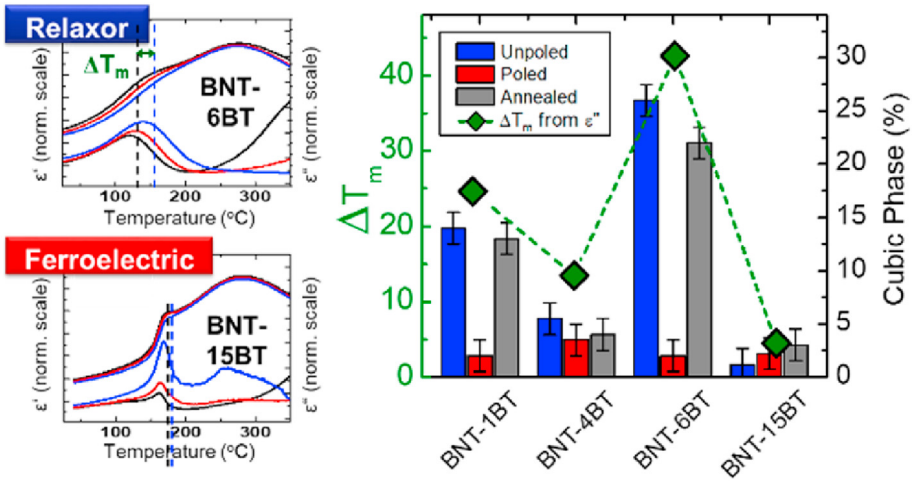

Fig. 13. Dielectric permittivity as a function of temperature for relaxor and ferroelectric NBT-xBT, along with the correlation between its frequency dispersion and the cubic phase content found by means of ^{23}Na MAS NMR.

after field cooling relaxor samples. It could also be observed that the achieved ferroelectric state is unstable at higher temperatures, and collapses into a relaxor state at a temperature T_{F-R}, this temperature being composition dependent.

The comparison of these quadrupole-perturbed NMR lines of NBT-xBT samples before and after electrical poling reveals the coexistence of phases with cubic and polar symmetries for the samples found in a relaxor state (Fig. 12). The cubic portion vanishes when a ferroelectric state is induced, either by the application of an electric field or by composition changes (Fig. 13). This result supports a model of polar nanoregions (PNRs) embedded in a cubic non-polar matrix for the ground state of these lead-free relaxors, hence, helping to solve the long-standing open question about the structure of relaxor ferroelectrics.

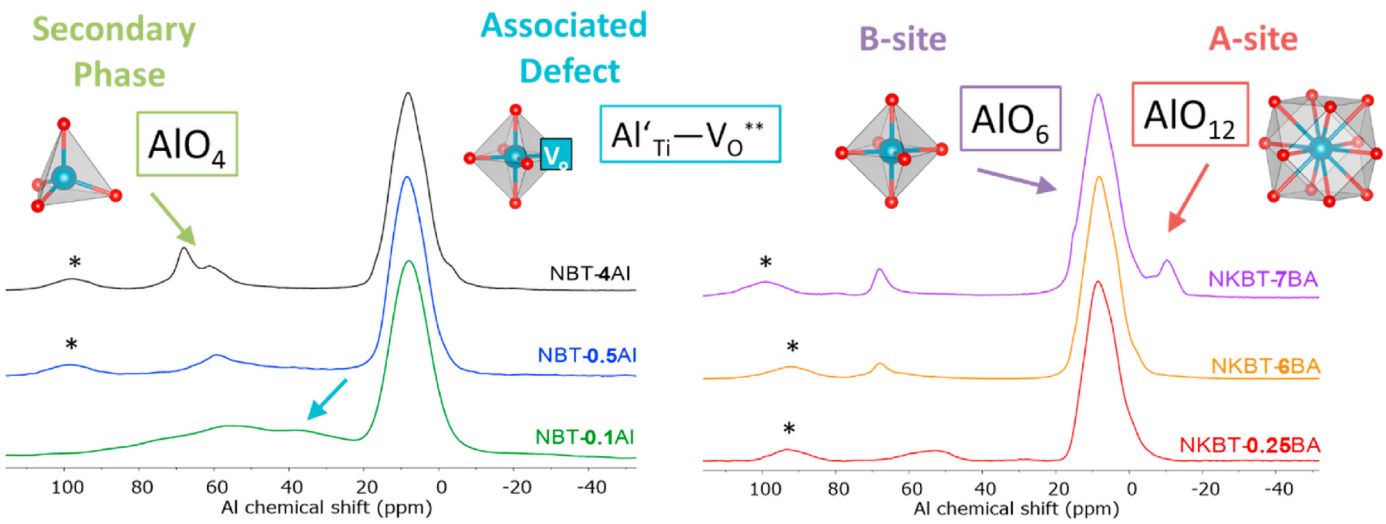

Fig. 14. ^{27}Al MAS NMR spectra of (a) Al acceptor-doped NBT and (b) NKBT-xBA solid solutions. Spinning sidebands marked with an asterisk. Magnetic field of 14.1 T (adapted from Ref. [96]).

3.3.5. *^{27}Al NMR spectroscopy*

The polymorphs of Al_2O_3 are an important source of aluminium for the preparation of oxides. α-Al_2O_3, which is isostructural with the mineral corundum, can be prepared either by calcination of the aluminium hydroxides bayesite or gibsite. A different dehydration path is followed for each hydroxide, where the polymorphs of Al_2O_3 (γ, κ, etc..), known as transition aluminas, might form. Corundum shows a single ^{27}Al NMR resonance located in the AlO_6 region of the spectra. Its isotropic chemical shift is equal to 16 ppm, and a quadrupolar coupling constant (C_Q) of 2.4 MHz is reported for it [104]. For γ-Al_2O_3, which is an amorphous transition alumina with high porosity, both AlO_6 and AlO_4 moieties are present at large content, with ^{27}Al NMR resonances at 9 ppm and 68 ppm, respectively [106]. A further polymorph, θ-Al_2O_3 also exhibits both coordination environments, with an isotropic chemical shift of 10 ppm and 80 ppm for the six- and four-fold coordinated sites [107]. κ-Al_2O_3 was investigated with NMR by Massiot et al. [108] and four different Al environments were found, two as AlO_6, one AlO_4 and a further, more distorted aluminium site. The C_Q values for the six-fold coordinated aluminium sites varied from 0.5 to 0.8 MHz (chemical shift of 13 an 18 ppm, respectively), whereas the four-fold coordinated site displayed a C_Q of 0.7 MHz. The more distorted site present upfield from the AlO_6 signals had a C_Q estimated to be around 1.5 MHz.

Aluminium is also found as the B-site cation of different perovskites. The local environment of aluminium in $LaAlO_3$ has been investigated with ^{27}Al NMR and indicates an almost cubic structure with very little distortion of the AlO_6 octahedra. As a consequence, a small C_Q of 0.12 MHz was observed for Al in this site, with an isotropic value of chemical shift equal to 11 ppm [109]. $YAlO_3$ has also been investigated with ^{27}Al NMR. Based on a single-crystal study, a more distorted local structure than that of $LaAlO_3$ was identified, with a C_Q of 1.5 MHz [110]. Despite that, not very large differences are expected for the chemical shift value of aluminium poised in the B-site of perovskites, as a chemical shift of 10 ppm has been calculated with DFT for $YAlO_3$ [111].

There are also reports on $YAlO_3$ in solid-solutions with alkaline earth metals [112]. In case Sr^{2+} is added to the A-site, a second signal develops besides the typical AlO_6 signal, namely a signal in the tetragonal region of the ^{27}Al NMR spectra [113]. In this report, the AlO_4 was attributed to the formation of oxygen vacancies, however no sign of a AlO_5 site was observed, which is expected from association of V_O** with the aluminium site.

Aluminium can be also present as a minor component in perovskite materials. The aluminium substitution in $MgSiO_3$ was thoroughly investigate with ^{27}Al NMR by Stebbins [114]. They observed Al^{3+} is majorly present in the B-site, with chemical shift of 6 ppm and a C_Q of 1 MHz. Aluminium was also found as a substituent in the A-site, with chemical shift of −7 ppm and a large C_Q of 7 MHz. This was attributed to the small ionic radii of Mg^{2+} and Si^{4+}. In addition to these sites, a third aluminium environment was observed, which resonance occurs at 15 ppm with a C_Q around 2 MHz. This signal is located on the edge of the AlO6 region of chemical shift, and was hence assigned to AlO_5 moieties. The penta-coordinated aluminium site was proposed as aluminium located in the B-site associated with an oxygen vacancy, whence its chemical shift being close to the AlO_6 region of ^{27}Al NMR spectra. Despite this explanation, this assignment is somewhat controversial, as the signal of corundum occurs in a similar chemical shift value.

3.3.6. *Local environment of acceptor dopants in NBT [96]*

Acceptor doping in perovskite oxides has a paramount influence on functional properties including ionic conductivity and piezoelectricity. Although its mechanism of action is often attributed to the formation of defect pairs (e.g. [Al_{Ti}-V_O]*) between the acceptor dopant and oxygen vacancies, there is still a lack of evidence for such associated defects in the literature, as far as diamagnetic ions are concerned.

Groszewicz et al. employed a combination of ^{27}Al NMR spectroscopy and DFT calculations in order to clarify the presence of associated defects in Al-doped ($(Na_{1/2},Bi_{1/2})TiO_3$ (NBT-Al) and Al-substituted solid-solutions of $(Na,K)_{1/2}Bi_{1/2})TiO_3$ –$BiAlO_3$ (NKBT-BA) [96]. This combination of techniques is able to reveal the fate of aluminium in (Na,Bi)TiO_3-based perovskites for samples with an Al^{3+} content as low as 0.1%. Furthermore, structure-property relations concerning the ionic conductivity were also described.

Different local environments of Al^{3+} in NBT were calculated with DFT along with computed chemical shift values, to serve as a fingerprint of the possible sites for aluminium in the structure. These ranged from potential secondary phases with tetragonal local environment, to the B-site of the perovskite structure, both with and without associated oxygen vacancies, and its A-site.

^{27}Al MAS NMR spectra for NBT-Al (Fig. 14) exhibit a signal at +8 ppm, characterized as the regular B-site. In addition to that, AlO_4 moieties attributed to secondary phases are omnipresent. A signal assigned to the [Al_{Ti}-V_O]* associated defect was detected in the chemical shift region of pentacoordinated aluminium for the NBT sample with the lowest Al^{3+} content (0.1%). Its presence correlates to the low conductivity of this composition when compared to the remaining ones with higher dopant concentration. This observation was rationalized by a tendency for disassociation at higher doping, which explains the higher conductivity by the increased number of free mobile charge carriers.

For NKBT-BA compositions, which are considered from piezoelectric applications, no sign of associated defects is found. This correlates with the stoichiometry of the solid-solution, which compensates charges by additional Bi^{3+} content instead of having Al^{3+} solely as an acceptor dopant. Furthermore, compositions with a $BiAlO_3$ content higher than 7% displayed evidence for the occupation of the A-site as well, which is remarkable given the small radius of this cation, and defines the solubility limit for these solid-solutions [96].

4. Conclusion

This review presents a comprehensive collection of applications of Nuclear Magnetic Resonance (NMR) spectroscopy to the study of the local structure of lead-free perovskites oxides, along with its distortions and the effects of structural disorder. Examples from NMR of ^{23}Na, ^{137}Ba, $^{47,49}Ti$, ^{27}Al and ^{93}Nb for the structural analysis of solid-solutions based on $BaTiO_3$, $NaNbO_3$ and $Na_{1/2}Bi_{1/2}TiO_3$ are described. The selected materials comprise the main classes of lead-free piezoelectrics, but are also studied as prototypes of ferroelectric, relaxor, antiferroelectric materials, as well as potential ceramic ionic conductors. Instead of offering a mathematically-dense description, the base concepts and capabilities of the technique are introduced by exploring tangible examples of application to electroceramics from a materials perspective. In this way, it offers a new and unique approach to the topic and aims at increasing the awareness among the electroceramics and materials science communities.

Declaration of competing interest

The author declares he has no known competing financial interests or personal relationships that could have appeared to influence the work reported in this paper.

Acknowledgement

P.G. gratefully acknowledges financial support by the Dutch Research Council (NWO) for the ECCM Tenure Track funding under project number ECCM.006, as well as the Deutsche Forschungsgemeinschaft (DFG) under contract Bu-911-28-1. The author kindly acknowledges the collaborative work with the research groups of Prof. Gerd Buntkowsky and Prof. Jürgen Rödel (NAW) at the TU Darmstadt, as well as Dr. Hergen Breitzke for instructive discussions about NMR.

References

[1] G.H. Haertling, Ferroelectric ceramics: history and technology, J. Am. Ceram. Soc. 82 (1999) 797–818.
[2] J. Rödel, W. Jo, K.T.P. Seifert, E.-M. Anton, T. Granzow, D. Damjanovic, Perspective on the development of lead-free piezoceramics, J. Am. Ceram. Soc. 92 (2009) 1153–1177.
[3] J. Rödel, K.G. Webber, R. Dittmer, W. Jo, M. Kimura, D. Damjanovic, Transferring lead-free piezoelectric ceramics into application, J. Eur. Ceram. Soc. 35 (2015) 1659–1681.
[4] M. Acosta, N. Novak, V. Rojas, S. Patel, R. Vaish, J. Koruza, G.A. Rossetti, J. Rödel, BaTiO3-based piezoelectrics: fundamentals, current status, and perspectives, Appl. Phys. Rev. 4 (2017), 41305.
[5] H. Eckert, Spying with spins on messy materials: 60 Years of glass structure elucidation by NMR spectroscopy, Int. J. Appl. Glass Sci. 9 (2018) 167–187.
[6] A. Abragam, The Principles of Nuclear Magnetism, Clarendon Press, Oxford, 1970.
[7] N.J. Stone, TABLE OF NUCLEAR MAGNETIC DIPOLE AND ELECTRIC QUADRUPOLE MOMENTS, INDC International Nuclear Data Committee, 2014.
[8] N.J. Stone, New table of recommended nuclear electric quadrupole moments, Hyperfine Interact. 230 (2015) 7–16.
[9] D.I. Hoult, The NMR receiver: a description and analysis of design, Prog. Nucl. Magn. Reson. Spectrosc. 12 (1978) 41–77.
[10] M.H. Levitt, Spin Dynamics: Basics of Nuclear Magnetic Resonance, second ed., Wiley2013.
[11] T. Gutmann, P.B. Groszewicz, G. Buntkowsky, Chapter one - solid-state NMR of nanocrystals, in: G.A. Webb (Ed.) Annual Reports on NMR Spectroscopy, Academic Press2019, pp. 1-82.
[12] F. Bloch, Nuclear Induction, Physical Review 70 (1946) 460–474.
[13] H. Kirchhain, J. Holzinger, A. Mainka, A. Spörhase, S. Venkatachalam, A. Wixforth, L. van Wüllen, High-temperature MAS-NMR at high spinning speeds, Solid State Nucl. Magn. Reson. 78 (2016) 37–39.
[14] O. Pecher, J. Carretero-González, K.J. Griffith, C.P. Grey, Materials' methods: NMR in battery research, Chem. Mater. 29 (2017) 213–242.
[15] M.S. Vinding, T.O. Kessler, T. Vosegaard, A simple low-cost single-crystal NMR setup, J. Magn. Reson. 269 (2016) 120–127.
[16] N.R. Jaegers, K.T. Mueller, Y. Wang, J.Z. Hu, Variable temperature and pressure operando MAS NMR for catalysis science and related materials, Acc. Chem. Res. 53 (2020) 611–619.
[17] P. Groszewicz, H. Breitzke, G. Buntkowsky, Compensating the asymmetric probe response in broad MAS NMR spectra of quadrupolar nuclei, Solid State Nucl. Magn. Reson. 84 (2017) 227–233.
[18] E. Fukushima, S.B.W. Roeder, Experimental Pulse NMR : a Nuts and Bolts Approach, Addison-Wesley1981.
[19] C.P. Slichter, Principles of Magnetic Resonance, Springer, 1978.
[20] H. Friebolin, Ein- und zweidimensionale NMR-Spektroskopie, Wiley-VCH Verlag, Weinheim, 1992.
[21] D. Freude, J. Haase, Quadrupole Effects in Solid-State Nuclear Magnetic Resonance, Springer-Verlag, Berlin, 1993.
[22] W. Strojek, M. Kalwei, H. Eckert, Dipolar NMR strategies for multispin systems involving quadrupolar Nuclei: 31P{23Na} rotational echo double resonance (REDOR) of crystalline sodium phosphates and phosphate glasses, J. Phys. Chem. B 108 (2004) 7061–7073.
[23] D. Massiot, F. Fayon, M. Deschamps, S. Cadars, P. Florian, V. Montouillout, N. Pellerin, J. Hiet, A. Rakhmatullin, C. Bessada, Detection and use of small J couplings in solid state NMR experiments, Compt. Rendus Chem. 13 (2010) 117–129.
[24] A.J. Pell, G. Pintacuda, C.P. Grey, Paramagnetic NMR in solution and the solid state, Prog. Nucl. Magn. Reson. Spectrosc. 111 (2019) 1–271.
[25] R.F. Moran, D.M. Dawson, S.E. Ashbrook, Exploiting NMR spectroscopy for the study of disorder in solids, Int. Rev. Phys. Chem. 36 (2017) 39–115.
[26] H. Sung, Choh, H. Shin, I.-W. Park, h. ju, J. Kim, Calculation of electric field gradient tensor for simple point charge distributions and its application to real systems, Journal of the Korean Magnetic Resonance Society 7 (2003) 16–24.
[27] C.J. Pickard, F. Mauri, All-electron magnetic response with pseudopotentials: NMR chemical shifts, Phys. Rev. B 63 (2001), 245101.
[28] J.R. Yates, C.J. Pickard, F. Mauri, Calculation of NMR chemical shifts for extended systems using ultrasoft pseudopotentials, Phys. Rev. B 76 (2007), 24401.
[29] J.-P. Amoureux, M. Pruski, MQMASNMR: Experimental Strategies and Applications, eMagRes, John Wiley & Sons, Ltd, 2007.
[30] D. Massiot, F. Fayon, M. Capron, I. King, S. Le Calvé, B. Alonso, J.-O. Durand, B. Bujoli, Z. Gan, G. Hoatson, Modelling one- and two-dimensional solid-state NMR spectra, Magn. Reson. Chem. 40 (2002) 70–76.
[31] M. Bak, J.T. Rasmussen, N.C. Nielsen, SIMPSON: a general simulation program for solid-state NMR spectroscopy, J. Magn. Reson. 147 (2000) 296–330.
[32] L.J. Mueller, Tensors and rotations in NMR, Concepts Magn. Reson. 38A (2011) 221–235.
[33] P. van der Wel, Use of solid-state NMR spectroscopy for investigating polysaccharide-based hydrogels: a review, Carbohydr. Polym. 240 (2020), 116276.
[34] J.W. Hennel, J. Klinowski, Magic-angle spinning: a historical perspective, in: J. Klinowski (Ed.), New Techniques in Solid-State NMR, Springer Berlin Heidelberg, Berlin, Heidelberg, 2005, pp. 1–14.
[35] Z. Gan, Satellite transition NMR spectroscopy of half-integer quadrupolar nuclei under magic-angle spinning, in: Encyclopedia of Nuclear Magnetic Resonance, J. Wiley, Chichester, 2002, p. 132.
[36] H. Thurnauer, J. Deaderick, Insulating Material, Google Patents, 1947.
[37] A. von Hippel, R.G. Breckenridge, F.G. Chesley, L. Tisza, High dielectric constant ceramics, Ind. Eng. Chem. 38 (1946) 1097–1109.
[38] B. Jaffe, W.R. Cook Jr., H. Jaffe, Piezoelectric Ceramics, Academic Press, 1971.
[39] H.F. Kay, P. Vousden, XCV. Symmetry changes in barium titanate at low temperatures and their relation to its ferroelectric properties, the London, Edinburgh, and Dublin, Philosophical Magazine and Journal of Science 40 (1949) 1019–1040.
[40] H.D. Megaw, Crystal structure of barium titanate, Nature 155 (1945).
[41] G. Shirane, H. Danner, R. Pepinsky, Neutron diffraction study of orthorhombic BaTiO3, Phys. Rev. 105 (1957) 856–860.
[42] A.W. Hewat, Structure of rhombohedral ferroelectric barium titanate, Ferroelectrics 6 (1973) 215–218.
[43] T.J. Bastow, H.J. Whitfield, 137Ba and 47,49Ti NMR: electric field gradients in the non-cubic phases of BaTiO3, Solid State Commun. 117 (2001) 483–488.
[44] O. Kanert, H. Schulz, J. Albers, Nuclear magnetic resonance study of the cubic-to-tetragonal phase transition in BaTiO3, Solid State Commun. 91 (1994) 465–469.
[45] P.P. Man, Quadrupole Couplings in Nuclear Magnetic Resonance, General, Encyclopedia of Analytical Chemistry.
[46] T.J. Bastow, An NMR study of137Ba and47,49Ti in ferroelectric BaTiO3, J. Phys. Condens. Matter 1 (1989) 4985–4991.

[47] T.J. Bastow, P.J. Dirken, M.E. Smith, H.J. Whitfield, Factors controlling the 17O NMR chemical shift in ionic mixed metal oxides, J. Phys. Chem. 100 (1996) 18539–18545.

[48] P. Zhao, S. Prasad, J. Huang, J.J. Fitzgerald, J.S. Shore, Lead-207 NMR spectroscopic study of lead-based electronic materials and related lead oxides, J. Phys. Chem. B 103 (1999) 10617–10626.

[49] F. Fayon, I. Farnan, C. Bessada, J. Coutures, D. Massiot, J.P. Coutures, Empirical correlations between 207Pb NMR chemical shifts and structure in solids, J. Am. Chem. Soc. 119 (1997) 6837–6843.

[50] S.F. Dec, M.F. Davis, G.E. Maciel, C.E. Bronnimann, J.J. Fitzgerald, S.S. Han, Solid-state multinuclear NMR studies of ferroelectric, piezoelectric, and related materials, Inorg. Chem. 32 (1993) 955–959.

[51] K.J.D. MacKenzie, R.H. Meinhold, Prospects for 137Ba MAS NMR spectroscopy of ceramics and related inorganic materials, Ceram. Int. 26 (2000) 87–92.

[52] E.N. Bunting, G.R. Shelton, A.S. Creamer, Properties OF barium-strontium titanate dielectrics*, J. Am. Ceram. Soc. 30 (1947) 114–125.

[53] C. Gervais, D. Veautier, M.E. Smith, F. Babonneau, P. Belleville, C. Sanchez, Solid state 47,49Ti, 87Sr and 137Ba NMR characterisation of mixed barium/strontium titanate perovskites, Solid State Nucl. Magn. Reson. 26 (2004) 147–152.

[54] J.-P. Amoureux, M. Pruski, MQMASNMR: Experimental Strategies and Applications, John Wiley & Sons, Ltd, 2007.

[55] G. Czjzek, J. Fink, F. Götz, H. Schmidt, J.M.D. Coey, J.P. Rebouillat, A. Liénard, Atomic coordination and the distribution of electric field gradients in amorphous solids, Phys. Rev. B 23 (1981) 2513–2530.

[56] G.L. Caër, B. Bureau, D. Massiot, An extension of the Czjzek model for the distributions of electric field gradients in disordered solids and an application to NMR spectra of71Ga in chalcogenide glasses, J. Phys. Condens. Matter 22 (2010), 65402.

[57] K. Wang, J.-F. Li, K. Na, NbO3-based lead-free piezoceramics: phase transition, sintering and property enhancement, Journal of Advanced Ceramics 1 (2012) 24–37.

[58] B. Malic, J. Koruza, J. Hrescak, J. Bernard, K. Wang, J.G. Fisher, A. Bencan, Sintering of lead-free piezoelectric sodium potassium niobate ceramics, Materials 8 (2015) 8117–8146.

[59] H. Shimizu, H. Guo, S.E. Reyes-Lillo, Y. Mizuno, K.M. Rabe, C.A. Randall, Lead-free Antiferroelectric: xCaZrO3-(1 − x)NaNbO3 system (0 ≤ x ≤ 0.10), Dalton Trans. 44 (2015) 10763–10772.

[60] D. Yang, J. Gao, L. Shu, Y.-X. Liu, J. Yu, Y. Zhang, X. Wang, B.-P. Zhang, J.-F. Li, Lead-free antiferroelectric niobates AgNbO3 and NaNbO3 for energy storage applications, J. Mater. Chem. 8 (2020) 23724–23737.

[61] H. Zhang, T. Wei, Q. Zhang, W. Ma, P. Fan, D. Salamon, S.-T. Zhang, B. Nan, H. Tan, Z.-G. Ye, A review on the development of lead-free ferroelectric energy-storage ceramics and multilayer capacitors, J. Mater. Chem. C 8 (2020) 16648–16667.

[62] F. Zhuo, H. Qiao, J. Zhu, S. Wang, Y. Bai, X. Mao, H.-H. Wu, Perspective on antiferroelectrics for energy storage and conversion applications, Chin. Chem. Lett. (2020), https://doi.org/10.1016/j.cclet.2020.11.070.

[63] B.T. Matthias, New ferroelectric crystals, Phys. Rev. 75 (1949), 1771–1771.

[64] H.D. Megaw, 7 phases of sodium niobate, Ferroelectrics 7 (1974) 87–89.

[65] A.C. Sakowski-Cowley, K. Lukaszewicz, H.D. Megaw, The structure of sodium niobate at room temperature, and the problem of reliability in pseudosymmetric structures, Acta Crystallogr. B 25 (1969) 851–865.

[66] A. Weiss, Das Resonanzspektrum des Kernspins von 23Na in Einkristallen von Natriumnitrit, NaNO2, Zeitschrift für Naturforschung A, 1960, p. 15a.

[67] H. Koller, G. Engelhardt, A.P.M. Kentgens, J. Sauer, 23Na NMR spectroscopy of solids: interpretation of quadrupole interaction parameters and chemical shifts, J. Phys. Chem. 98 (1994) 1544–1551.

[68] R.K. Harris, E.D. Becker, S.M. Cabral de Menezes, P. Granger, R.E. Hoffman, K.W. Zilm, Further conventions for NMR shielding and chemical shifts (IUPAC recommendations 2008), Ann. Magn. Reson. 7 (2008) 1–31.

[69] S.E. Ashbrook, L. Le Polles, R. Gautier, C.J. Pickard, R.I. Walton, 23Na multiple-quantum MAS NMR of the perovskites NaNbO3 and NaTaO3, Phys. Chem. Chem. Phys. 8 (2006) 3423–3431.

[70] X. Xue, J. Stebbins, 23Na NMR chemical shifts and local Na coordination environments in silicate crystals, melts and glasses, Phys. Chem. Miner. 20 (1993) 297–307.

[71] J.F. Stebbins, A.M. George, High-temperature 23Na MAS NMR data for albite: comparison to chemical-shift models, Am. Mineral. 80 (1995).

[72] F. Angeli, J.M. Delaye, T. Charpentier, J.C. Petit, D. Ghaleb, P. Faucon, Influence of glass chemical composition on the Na–O bond distance: a 23Na 3Q-MAS NMR and molecular dynamics study, J. Non-Cryst. Solids 276 (2000) 132–144.

[73] K.E. Johnston, C.C. Tang, J.E. Parker, K.S. Knight, P. Lightfoot, S.E. Ashbrook, The polar phase of NaNbO3: a combined study by powder diffraction, solid-state NMR, and first-principles calculations, J. Am. Chem. Soc. 132 (2010) 8732–8746.

[74] H. Shimizu, H.Z. Guo, S.E. Reyes-Lillo, Y. Mizuno, K.M. Rabe, C.A. Randall, Lead-free antiferroelectric: xCaZrO(3)-(1-x)NaNbO3 system (0 <= x <= 0.10), Dalton Trans. 44 (2015) 10763–10772.

[75] F. Wolf, D. Kline, H.S. Story, 93Nb and 23Na NMR in polycrystalline sodium niobate, J. Chem. Phys. 53 (1970) 3538-+.

[76] K.E. Johnston, J.M. Griffin, R.I. Walton, D.M. Dawson, P. Lightfoot, S.E. Ashbrook, 93Nb NMR and DFT investigation of the polymorphs of NaNbO3, Phys. Chem. Chem. Phys. 13 (2011) 7565–7576.

[77] J. Koruza, P. Groszewicz, H. Breitzke, G. Buntkowsky, T. Rojac, B. Malič, Grain-size-induced ferroelectricity in NaNbO3, Acta Mater. 126 (2017) 77–85.

[78] S. Egert, M.-H. Zhang, J. Koruza, P.B. Groszewicz, G. Buntkowsky, 23Na NMR spectroscopic quantification of the antiferroelectric–ferroelectric phase coexistence in sodium niobate, J. Phys. Chem. C 124 (2020) 23852–23858.

[79] M.-H. Zhang, L. Fulanović, S. Egert, H. Ding, P.B. Groszewicz, H.-J. Kleebe, L. Molina-Luna, J. Koruza, Electric-field-induced antiferroelectric to ferroelectric phase transition in polycrystalline NaNbO3, Acta Mater. 200 (2020) 127–135.

[80] M.-H. Zhang, N. Hadaeghi, S. Egert, H. Ding, H. Zhang, P.B. Groszewicz, G. Buntkowsky, A. Klein, J. Koruza, Design of Lead-Free Antiferroelectric (1 – x) NaNbO3–xSrSnO3 compositions guided by first-principles calculations, Chem. Mater. 33 (2021) 266–274.

[81] V.V. Shvartsman, D.C. Lupascu, Lead-free relaxor ferroelectrics, J. Am. Ceram. Soc. 95 (2012) 1–26.

[82] A.R. Paterson, H. Nagata, X. Tan, J.E. Daniels, M. Hinterstein, R. Ranjan, P.B. Groszewicz, W. Jo, J.L. Jones, Relaxor-ferroelectric transitions: sodium bismuth titanate derivatives, MRS Bull. 43 (2018) 600–606.

[83] M. Li, M.J. Pietrowski, R.A. De Souza, H. Zhang, I.M. Reaney, S.N. Cook, J.A. Kilner, D.C. Sinclair, A family of oxide ion conductors based on the ferroelectric perovskite Na0.5Bi0.5TiO3, Nat. Mater. 13 (2014) 31–35.

[84] S.-T. Zhang, A.B. Kounga, E. Aulbach, H. Ehrenberg, J. Rödel, Giant strain in lead-free piezoceramics Bi0.5Na0.5TiO3–BaTiO3–K0.5Na0.5NbO3 system, Appl. Phys. Lett. 91 (2007), 112906.

[85] T. Takenaka, K. Maruyama, K. Sakata, (Bi1/2Na1/2)TiO3-BaTiO3 system for lead-free piezoelectric ceramics, Jpn. J. Appl. Phys. 30 (1991) 2236.

[86] W. Jo, J.E. Daniels, J.L. Jones, X. Tan, P.A. Thomas, D. Damjanovic, J. Rödel, Evolving morphotropic phase boundary in lead-free (Bi1/2Na1/2)TiO3–BaTiO3 piezoceramics, J. Appl. Phys. 109 (2011), 14110.

[87] C. Ma, X. Tan, apos Dul, E. kin, M. Roth, Domain structure-dielectric property relationship in lead-free (1−x)(Bi1/2Na1/2)TiO3 xBaTiO3 ceramics, J. Appl. Phys. 108 (2010), 104105.

[88] R. Ranjan, A. Dviwedi, Structure and dielectric properties of (Na0.50Bi0.50) 1−xBaxTiO3: 0≤x≤0.10, Solid State Commun. 135 (2005) 394–399.

[89] B.N. Rao, A.N. Fitch, R. Ranjan, Ferroelectric-ferroelectric phase coexistence in Na1/2Bi1/2TiO3, Phys. Rev. B 87 (2013), 60102.

[90] W. Jo, S. Schaab, E. Sapper, L.A. Schmitt, H.-J. Kleebe, A.J. Bell, J. Rödel, On the phase identity and its thermal evolution of lead free (Bi1/2Na1/2)TiO3-6 mol% BaTiO3, J. Appl. Phys. 110 (2011), 74106.

[91] J. Suchanicz, The low-frequency dielectric relaxation Na0.5Bi0.5TiO3 ceramics, Mater. Sci. Eng., B 55 (1998) 114–118.

[92] I.P. Aleksandrova, A.A. Sukhovsky, Y.N. Ivanov, Y.E. Yablonskaya, S.B. Vakhrushev, Local and average structure of relaxor Na1/2Bi1/2TiO3 from the point of view of NMR, Ferroelectrics 378 (2009) 16–22.

[93] P.B. Groszewicz, H. Breitzke, R. Dittmer, E. Sapper, W. Jo, G. Buntkowsky, J. Rödel, Nanoscale phase quantification in lead-free ${{\mathrm{Bi}}_{1/2}{\mathrm{Na}}_{1/2}}{\mathrm{TiO}}_{3}\text{\ensuremath{-}}{\mathrm{BaTiO}}_{3}$ relaxor ferroelectrics by means of $^{23}\mathrm{Na}$ NMR, Phys. Rev. B 90 (2014), 220104.

[94] P.B. Groszewicz, M. Gröting, H. Breitzke, W. Jo, K. Albe, G. Buntkowsky, J. Rödel, Reconciling local structure disorder and the relaxor state in (Bi1/2Na1/2)TiO3-BaTiO3, Sci. Rep. 6 (2016) 31739.

[95] P.B. Groszewicz, H. Breitzke, W. Jo, J. Rödel, G. Buntkowsky, Local structure of the B-site in BNT-xBT investigated by 47,49Ti NMR: effect of barium content, J. Appl. Phys. 121 (2017), 114104.

[96] P.B. Groszewicz, L. Koch, S. Steiner, A. Ayrikyan, K.G. Webber, T. Frömling, K. Albe, G. Buntkowsky, The fate of aluminium in (Na,Bi)TiO3-based ionic conductors, J. Mater. Chem. 8 (2020) 18188–18197.

[97] D. Viehland, S.J. Jang, L.E. Cross, M. Wuttig, Freezing of the polarization fluctuations in lead magnesium niobate relaxors, J. Appl. Phys. 68 (1990) 2916–2921.

[98] N. Hao, B.G. Sayer, G. Dénès, D.G. Bickley, C. Detellier, M.J. McGlinchey, Titanium-47 and -49 nuclear magnetic resonance spectroscopy: chemical applications, J. Magn. Reson. 50 (1969) 50–63.

[99] D. Padro, V. Jennings, M.E. Smith, R. Hoppe, P.A. Thomas, R. Dupree, Variations of titanium interactions in solid state NMRCorrelations to local structure, J. Phys. Chem. B 106 (2002) 13176–13185.

[100] D. Padro, A.P. Howes, M.E. Smith, R. Dupree, Determination of titanium NMR parameters of ATiO 3 compounds: correlations with structural distortion, Solid State Nucl. Magn. Reson. 15 (2000) 231–236.

[101] S.L. Patt, Pulse strategies for the suppression of acoustic ringing, J. Magn. Reson. 49 (1969) 161–163.

[102] D.G. Cory, W.M. Ritchey, Suppression of signals from the probe in bloch decay spectra, J. Magn. Reson. 80 (1969) 128–132.

[103] V.A. Shuvaeva, D. Zekria, A.M. Glazer, Q. Jiang, S.M. Weber, P. Bhattacharya, P.A. Thomas, Local structure of the lead-free relaxor ferroelectric BNT-BKT, Phys. Rev. B 71 (2005), 174114.

[104] J. Skibsted, N.C. Nielsen, H. Bildsøe, H.J. Jakobsen, Satellite transitions in MAS NMR spectra of quadrupolar nuclei, J. Magn. Reson. 95 (1969) 88–117.

[105] M.E. Smith, E.R.H. van Eck, Recent advances in experimental solid state NMR methodology for half-integer spin quadrupolar nuclei, Prog. Nucl. Magn. Reson. Spectrosc. 34 (1999) 159–201.

[106] M.H. Lee, C.-F. Cheng, V. Heine, J. Klinowski, Distribution of tetrahedral and octahedral A1 sites in gamma alumina, Chem. Phys. Lett. 265 (1997) 673–676.

[107] L.A. O'Dell, S.L.P. Savin, A.V. Chadwick, M.E. Smith, A 27Al MAS NMR study of a sol–gel produced alumina: identification of the NMR parameters of the θ-Al2O3 transition alumina phase, Solid State Nucl. Magn. Reson. 31 (2007) 169–173.

[108] B. Ollivier, R. Retoux, P. Lacorre, D. Massiot, G. Férey, Crystal structure of κ-alumina: an X-ray powder diffraction, TEM and NMR study, J. Mater. Chem. 7 (1997) 1049–1056.
[109] F. Blanc, D.S. Middlemiss, L. Buannic, J.L. Palumbo, I. Farnan, C.P. Grey, Thermal phase transformations in LaGaO3 and LaAlO3 perovskites: an experimental and computational solid-state NMR study, Solid State Nucl. Magn. Reson. 42 (2012) 87–97.
[110] D.P. Burum, R.M. Macfarlane, R.M. Shelby, L. Mueller, Temperature dependence of 27Al NMR in YAlO3, Phys. Lett. 91 (1982) 465–468.
[111] M. Choi, K. Matsunaga, F. Oba, I. Tanaka, 27Al NMR chemical shifts in oxide crystals: a first-principles study, J. Phys. Chem. C 113 (2009) 3869–3873.
[112] E.V. Charnaya, C. Tien, N.V. Chejina, M.K. Lee, S.Y. Sun, Effect of alkali-earth ions on the local structure of LaAlO3-La0.67A0.33MnO3 (A = Ca, Sr, Ba) diluted solid solutions: 27Al NMR studies, Phys. Solid State 49 (2007) 449.
[113] E. Lima, M.-E. Villafuerte-Castrejón, J.M. Saniger, A. Ibarra-Palos, J.E. Sánchez-Sánchez, L.J. Álvarez, Experimental XRD and NMR, and molecular dynamics study of Sr containing LaAlO3 perovskite, Solid State Ionics 178 (2008) 1944–1949.
[114] J.F. Stebbins, H. Kojitani, M. Akaogi, A. Navrotsky, Aluminum substitution in MgSiO3 perovskite: investigation of multiple mechanisms by 27Al NMR, Am. Mineral. 88 (2003) 1161–1164.